DISCLAIMER

ANL-AMMT-023

Microstructure-Based Understanding of High-Temperature Deformation Behaviors in Laser Powder Bed Fusion (LPBF) 316H Stainless Steel

Nuclear Science and Engineering Division

ANL-AMMT-023

Microstructure-Based Understanding of High-Temperature Deformation Behaviors in Laser Powder Bed Fusion (LPBF) 316H Stainless Steel

---

prepared by

Xuan Zhang, Yiren Chen, Lin Gao, Mark Messner
Argonne National Laboratory

Heramb Mahajan, Ninad Mohale, Malachi Nelson, Michael McMurtrey
Idaho National Laboratory

September 2025

ABSTRACT

This report presents the results of high-temperature mechanical property testing and microstructural analysis of laser powder bed fusion (LPBF) 316H stainless steel (SS) conducted during Fiscal Year 2025 (FY25) under the U.S. Department of Energy, Office of Nuclear Energy's Advanced Materials and Manufacturing Technologies (AMMT) program. The study builds upon prior work by expanding the mechanical property test matrix and advancing a microstructure-based mechanistic understanding of LPBF 316H SS performance, with a focus on the solution annealed (SA, 1100°C for 1 hour) materials. High-temperature tension, creep, fatigue, and creep-fatigue tests were performed. Thermal aging studies were conducted. Advanced characterization techniques, including scanning electron microscopy (SEM), scanning transmission electron microscopy (STEM), and high-energy synchrotron X-ray diffraction, were employed to investigate the microstructural evolution during thermal aging and mechanical testing.

It was discovered that the as-built (AB) LPBF 316H SS exhibited precipitation kinetics during thermal aging that are 10–100 times faster than its wrought counterpart due to the presence of high densities of preferred nucleation sites, while the precipitation kinetics in SA LPBF 316H was under investigation. The accelerated precipitation of embrittling phases such as sigma phase in LPBF 316H SS compared to its wrought counterpart led to significant impacts on creep ductility. The influence of laser printing parameters and build orientations on fatigue and creep-fatigue performance was observed. In assessing the creep-fatigue performance, it was discovered that the SA LPBF 316H samples failed in less than 200 cycles under 595°C, 0.5% (strain amplitude) with a 60-minute hold time.

This work establishes a mechanistic framework for predicting the long-term behavior of LPBF 316H SS, supporting its rapid qualification under the ASME BPVC. The findings contribute to the broader goal of enabling the deployment of advanced materials in next-generation nuclear energy systems. An outlook for FY26 work, including continued aging studies, mechanical testing, and microstructural characterization, is provided.

TABLE OF CONTENTS

LIST OF FIGURES

LIST OF TABLES

1 Introduction

Additive manufacturing (AM) has emerged as a transformative technology for the nuclear energy sector, being explored for its ability to incorporate innovative design, advance materials development, embed sensors for real-time monitoring, and so on. The U.S. Department of Energy (DOE), Office of Nuclear Energy (NE)'s Advanced Materials and Manufacturing Technologies (AMMT) program is at the forefront of these efforts, with the overarching goal of accelerating the development, qualification, and deployment of advanced materials and manufacturing technologies to ensure reliable and economical nuclear energy [1].

Among the materials under investigation, 316H stainless steel (SS) produced via laser powder bed fusion (LPBF) has been identified as a key candidate for high-temperature reactor applications. The 316H SS, a high-carbon variant of 316 SS, is known for its creep resistance and strength at elevated temperatures due to the formation of carbides during service. While the conventional wrought form of 316H SS is already qualified under the American Society of Mechanical Engineers (ASME) Boiler and Pressure Vessel Code (BPVC) Section III, Division 5 for Class A construction, the qualification of LPBF 316H SS remains a critical challenge. This qualification requires a comprehensive understanding of the process-microstructure-property relationships, as well as the development of a robust mechanical property database, including high-temperature tension, creep, fatigue, and creep-fatigue data.

In Fiscal Year 2024 (FY24), significant progress was made in understanding the high-temperature mechanical performance of LPBF 316H SS [2,3]. Research efforts focused on evaluating the effects of laser processing parameters, powder chemistry, and post-build heat treatments (e.g., stress relieving (SR), solution annealing (SA), and hot isostatic pressing (HIP)) on the microstructure and mechanical properties of the material. High-temperature mechanical testing, including creep, cyclic, and tensile tests, provided valuable insights into the performance of LPBF 316H SS under nuclear-relevant service conditions. These studies also highlighted the importance of addressing variability in machine systems, powder batches, and processing conditions to ensure consistent and reliable material performance.

Building on the accomplishments of FY24, the FY25 project continued to advance the understanding of LPBF 316H SS, with a dual focus on high-temperature mechanical property testing and microstructure-based mechanistic insights. The down-selection of a SA condition of 1100°C, 1 h was made for the first code case on LPBF 316H SS. The mechanical property database of SA LPBF 316H SS was then extended to cover a comprehensive tension, creep, fatigue and creep-fatigue test matrix on various builds. Thermal aging study was also underway. Advanced characterization was performed to understand microstructure-property correlations. This project, in combination with a companion computer modeling project, seeks to establish a mechanistic framework for predicting the long-term behavior of LPBF 316H SS from short-term experiments. These efforts will not only support the rapid qualification of LPBF 316H SS under the ASME BPVC but also contribute to the broader goal of enabling the deployment of advanced materials in next-generation nuclear energy systems.

This report provides the integrated results of tension (on aged samples), creep, fatigue, and creep-fatigue tests on LPBF 316H SS collected at Argonne National Laboratory (ANL) and Idaho National Laboratory (INL) between FY24 and FY25, along with the current state of microstructural-based understandings of the behaviors. An outlook for FY26 work is also provided.

2 Materials and methods

2.1 Materials

The materials studied in this work package were printed using five batches of 316H SS powders purchased under the AMMT program, as listed in Table 1. Four were from Praxiar Inc. (currently Linde plc), labeled as Prax-AM316H-1 to Prax-AM316H-4, and one was from Powder Alloy Corporation (PAC), labeled as PAC-AM316H-5. Their compositions, as provided by the manufacturers (Table 1), are within the range of UNS S31609 (316H SS) as specified in ASTM A213/A213M [4].

The materials were printed with different laser systems, namely Renishaw AM400, GE Concept Laser, and EOS M290. The machine, site, laser mode and printing parameters are listed in Table 2. The designations of corresponding builds are also provided. Post printing, some of the materials were solution annealed (SA) at 1100°C for 1 h, followed by water quenching.

Table 1. Chemical compositions of powders utilized in this study.

		ASTM UNS S31609	**316H powder**	**316H powder**	**316H powder**	**316H powder**	**316H powder**
Manufacturer			Praxair	Praxair	Praxair	Praxair	PAC
Designation		--	Prax-AM316H-1	Prax-AM316H-2	Prax-AM316H-3	Prax-AM316H-4	PAC-AM316H-5
Order quantity (kg)		- -	50	200	500	1000	200
Build designation			Not used in this study	ANL-B1; ORNL-ANL-best	ANL-B2; ORNL-B1; ORNL-B2; ORNL-B3	LANL-ANL-1; LANL-ANL-2; LANL-INL-2	LANL-INL-1
Composition (wt.%)	**Fe**	Bal.	Bal.	Bal.	Bal.	Bal.	Bal.
	Cr	16.0-18.0	17.6	16.8	17.0	16.7	16.94
	Ni	11.0-14.0	12.3	12.1	12.3	11.9	10.88
	Mo	2.00-3.00	2.6	2.5	2.3	2.6	2.23
	Mn	2.0*	1.03	1.13	1.05	0.02	1.02
	Si	1.00*	0.41	0.48	0.07	0.04	0.37
	C	0.04-0.10	0.05	0.06	0.08	0.07	0.043
	O	- -	0.05	0.03	0.03	0.02	0.048
	N	- -	0.01	0.01	0.01	0.01	0.05
	P	0.045*	<0.005	<0.005	<0.005	<0.005	0.031

	S	0.030*	0.00	0.00	0.00	0.00	0.001

* Maximum, unless a range or minimum is indicated.

Table 2. The machine, site, build designation, laser mode and printing parameters used in this study.

Lab/ machine	**Build designation**	**Laser mode**	**Laser Power (W)**	**Spot size (µm)**	**Scan speed (m/s)**	**Hatch spacing (µm)**	**Layer height (µm)**	**Rotation angle (°)**	**Energy density (J/mm^3)**
ANL/Renishaw AM400	ANL-B1; ANL-B2	Pulsed	195	70	0.67	110	50	67	53
ORNL/GE Concept Laser	ORNL-B1	Continuous	200	125	0.75	75	50	67	71
ORNL/GE Concept Laser	ORNL-B2	Continuous	290	130	1.5	75	50	67	52
ORNL/GE Concept Laser	ORNL-B3	Continuous	380	125	0.75	75	50	67	135
ORNL/Renishaw AM400	ORNL-ANL-best	Pulsed	195	70	0.67	110	50	67	53
LANL/EOS M290	LANL-ANL-1; LANL-ANL-2; LANL-INL-1; LANL-INL-2	Continuous	275	100	0.69	140	30	47	95

2.2 Thermal aging method

Materials were machined into SS-3 type tensile specimens for thermal aging experiment. Some specimens were extracted in the direction perpendicular to the build direction (BD) (Figure 1(a)), and the other has them in the direction parallel to BD (Figure 1(b)). The tensile specimens had nominally a gauge length of 7.62 mm, a gauge width of 1.52 mm and a gauge thickness of 0.76 mm. Individual specimens were wrapped in tantalum foils and encapsulated in quartz tubes under vacuum. For the batch of specimens machined out of a build named 20220603 (built with Prax-AM316H-1 powder), they were in as-built conditions. For the batch of specimens machined out of a build named 20230811 (built with Prax-AM316H-3 powder), they were solution annealed (1100°C, 1h) in quartz tube encapsulations. Those specimens were placed in box furnaces for thermal aging at 550°C, 650°C or 750°C. For each temperature, aging times varied in 5, 25, 100, 500, 2500, 10000 hours or even longer.

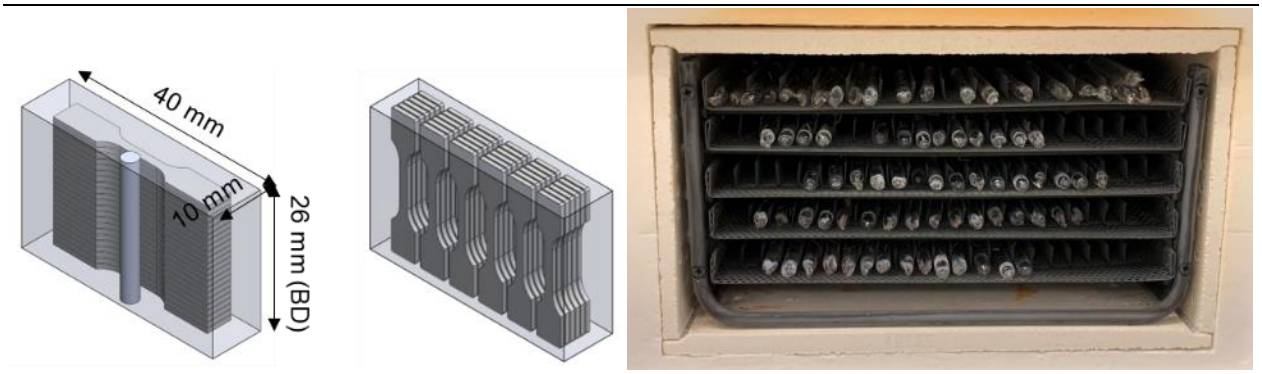

Figure 1. (a) A schematic showing the specimens extracted in the direction normal to BD (denoted as H orientation). (b) A schematic showing the specimens extracted in the direction parallel to BD (denoted as V orientation). (c) A photo showing the encapsulated specimens placed in a box furnace.

2.3 Mechanical testing methods

Uniaxial tension, creep, fatigue and creep-fatigue tests were performed on SA specimens. The specimens either have their gauge directions parallel to the BD (designated as "vertical specimens") or perpendicular to the BD (designated as "horizontal specimens").

2.3.1 Tension tests

Tension tests of subsized specimens were performed with two Instron Model 5980 Materials Testing Systems with the Instron Bluehill 3 testing software for control and data acquisition. Figure 2 provides the specimen dimensions. The testers are equipped with 3-zone furnaces for air testing up to 1100°C. To begin a test, a specimen was installed into a grip that was designed for shoulder loading. The tips of two thermal couples were placed in close vicinity to the top and bottom region of the gauge section of the specimen to reflect the actual temperature of the specimen and to serve as the input of the furnace control. The temperature was brought up to the target gradually and a soaking period of 1 hour was applied to ensure a thermal equilibrium of the loading train. All tests were conducted with a crosshead displacement rate of 0.00762 mm/s until rupture. The elastic modulus of the raw data was corrected with the known values of E = 200 GPa, 155 GPa, 146 GPa, and 134 GPa for 316 SS at RT, 550, 650 and 750°C, respectively [5].

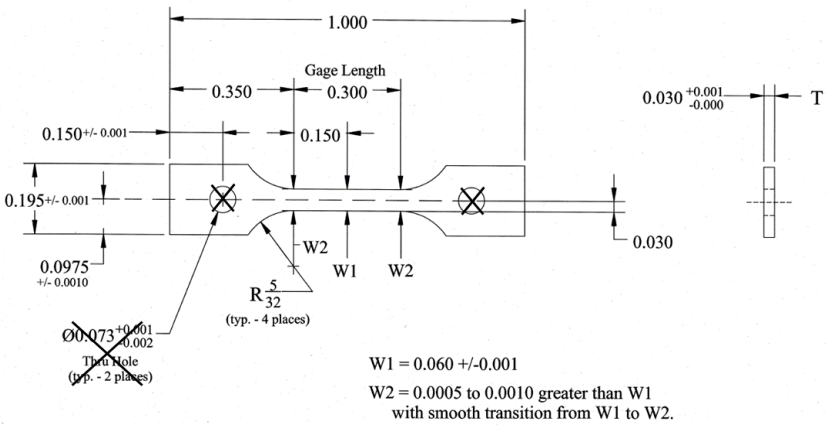

Figure 2. Subsized SS-3 type tension specimen geometry. The two pin holds are not machined for the specimens used in this study and are thus crossed out.

2.3.2 Creep tests

At ANL, the creep tests were performed in the Mechanical and Environmental Testing Laboratory and were conducted in accordance with ASTM E139 "Standard Test Methods for Conducting Creep, Creep Rupture, and Stress Rupture Tests of Metallic Materials". Figure 3 shows the specimen geometry. The frames were ATS Series 2300 Lever Arm Creep Testing Systems integrated with WinCCS II computer control and data acquisition software package. ATS systems are precision knife-edge lever arm testers. Each creep machine is equipped with a three-zone split-tube furnace capable of operation up to 1100°C. The temperature in the system is controlled by the ATS temperature control system which regulates the power applied to the resistive heating elements and maintains the desired temperature (setpoint) as measured by a control thermocouple. Type K thermocouples are used to measure the specimen temperatures, and when doing so, the two thermocouples are spot welded to the shoulder sections of the specimen and fed into the furnace control.

At INL, similarly, creep tests were conducted in accordance with ASTM E139 on Applied Test Systems lever arm creep frames, using a three-zone furnace for temperature control. For standard specimen testing, cylindrical test specimens similar to Figure 3 (b) were used with the longitudinal direction parallel to the build direction. Specimens had a 6.35-mm [0.250 in.] minimum diameter and a reduced parallel section that was at minimum 31.75-mm [1.250 in]. A modified test specimen geometry was used for sub-sized specimen testing that had a rectangular cross section that was 1.2 mm [0.047 in.] wide and either 0.5 mm [0.0197 in.] or 0.75 mm [0.0295 in.] thick. The reduced parallel section was 5 mm [0.197 in.] long.

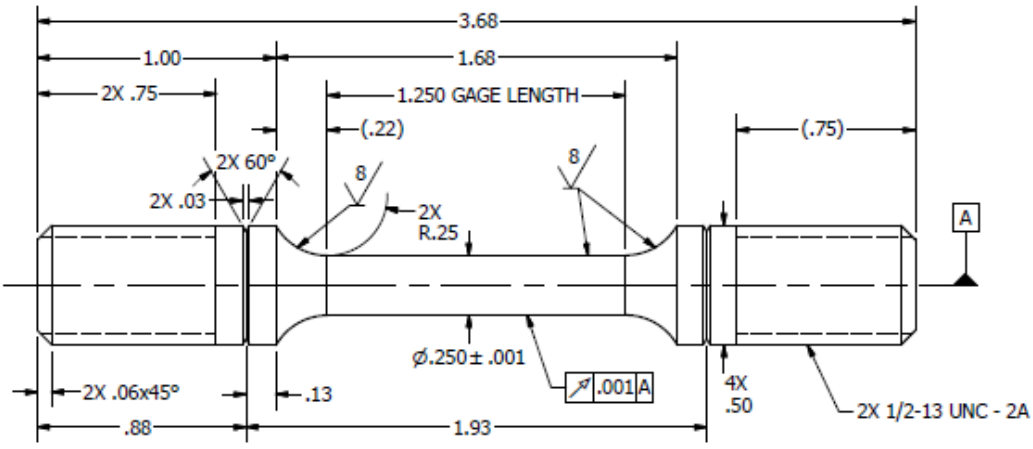

Figure 3. Dimensions of ANL creep specimens in ASTM standard geometry.

2.3.3 Fatigue and creep-fatigue tests

Fatigue and creep-fatigue tests were performed at ANL and INL on different AM builds in this study. While each laboratory used its own sample types and loading frames, the same test protocols and ASTM standards were followed for fatigue and creep tests as shown in Table 3. At ANL, a round bar specimen with a nominal gauge diameter of 5.5 mm (0.215 in.), a gauge length of 16.3 mm (0.64 in.), and a total length of 101.6 mm (4.0 in.), as shown in Figure 4, were used. Tests were carried out on two closed-loop servo-hydraulic test frames. Specimen heating was provided

by two three-zone split furnaces. The test temperature was controlled and monitored with two pairs of Type K thermocouples positioned at the top and bottom grip sections of the specimen. All the tests were conducted at 550°C in air. The fatigue tests were carried out under a constant strain amplitude in a fully reversed (R = -1) mode. A high-temperature extensometer was mounted at the uniform gauge section of the specimen to control the test. Both tension and compression strain rates were set at 0.001 s^{-1}. Creep-fatigue tests were performed using the same test systems and the same sample geometry as those used in the fatigue tests. To induce creep deformation, a hold time was applied at the peak tensile strain for each cycle. Instron WaveMatrix^{TM} Dynamic Software was used for test control and data acquisition. Stress-strain hysteresis loops and the maximum and minimum stresses were recorded periodically at different cycles throughout the test.

At INL, fatigue and creep-fatigue tests were performed on several MTS servo-hydraulic test frames, using three-zone furnaces for temperature control. The tests were also conducted in a strain-controlled mode with a fully reversed (R = -1) strain range of 1%. A triangular strain wave-form and a strain rate of 0.001 s^{-1} were used for all tests. Cylindrical test specimens were machined with their longitudinal direction parallel to the build direction. Specimens tested at INL had a 7.49-mm (0.29 in.) minimum diameter and a 20.0-mm (0.79 in.) parallel gauge section. The extensometer used at INL had a gauge length of 12 mm (0.47 in.). Creep-fatigue tests were performed using the same specimen geometry and extensometer. The tests were also fully reversed, but a hold time was implemented at peak tensile strain. The cyclic life was defined as the number of cycles when a drop of 20% in the ratio of peak and valley (maximum and minimum) stresses was detected.

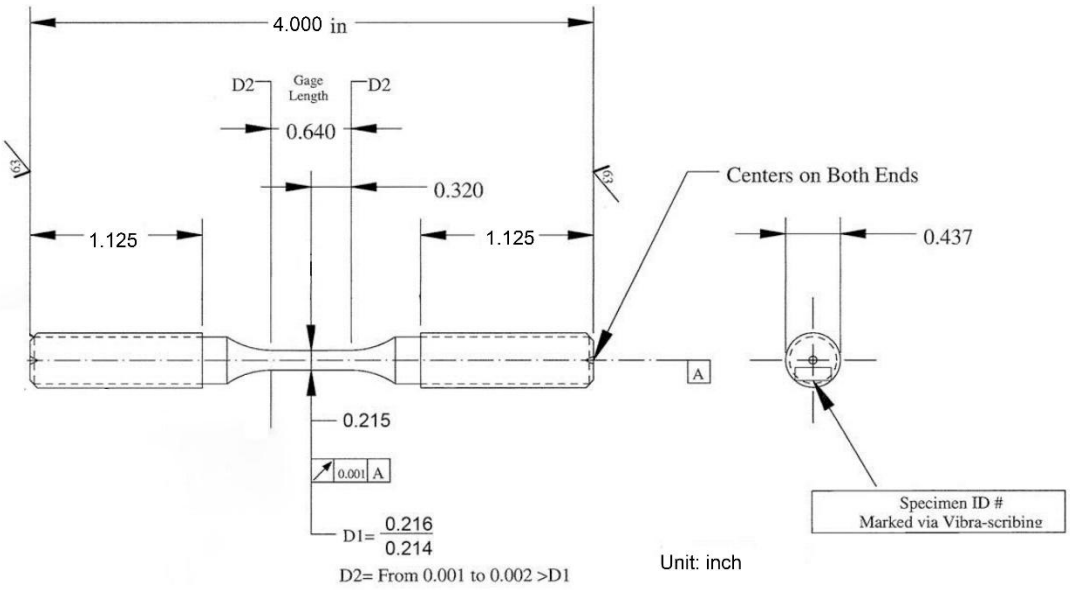

Figure 4 Round bar specimens used at ANL for the fatigue and creep-fatigue tests

Table 3. Fatigue and creep-fatigue tests performed at ANL and INL

	Sample		Test method	Strain rate	Test standard	
	Gauge length	Gauge dia.			Fatigue	Creep-fatigue
ANL	0.64”	0.215”	Strain controlled, R=-1	0.1%/s	E606/606M	E2714
INL	0.79”	0.29”	Strain controlled, R=-1	0.1%/s	E606/606M	E2714

2.4 Characterization

Scanning electron microscopy (SEM) was performed with a JEOL IT800HL microscope. Specimen surfaces were mechanically polished to mirror finish and final polished with a Buehler VibroMet system in 0.06-μm silica suspension. Electron beam voltages of 5-15 keV were used in those experiments. Both secondary electron detector (SED) imaging and backscattered electron (BSE) imaging were used to highlight different features. Electron backscatter diffraction (EBSD) and energy dispersive x-ray spectroscopy (EDS) were performed on selected specimens to provide quantitative information on grain structures and secondary phases.

Scanning transmission electron microscopy (STEM) in high-angle annular dark field (HAADF) and bright field (BF) imaging modes were performed with a FEI Talos F200X TEM/STEM at the Center for Nanoscale Materials (CNM) in ANL to study the microstructures of selected specimens. Specimens were mechanically polished down to 100 μm in thickness, and 3 mm TEM disks were punched out. The disks were then jet-polished until electron transparent with an electrolyte of 5% perchloric acid and 95% methanol at −30 °C with a Struers TenuPol-5 jet polisher. EDS was used to map the chemical composition of selected areas of interest. The EDS intensity maps were converted to Quantitative Hyperspectral X-ray Maps (Q-maps) for analysis.

3 Thermal aging of as-built LPBF 316H

3.1 Introduction

The assessment of long-term thermal stability for structural alloys is critical for the safe operation of high-temperature nuclear reactors, which have projected life spans of 40-60 years. To account for the loss of mechanical strength due to prolonged exposure to high temperatures, the American Society of Mechanical Engineers (ASME) Boiler and Pressure Vessel (BPV) code Section III, Division 5 [6], which provides high-temperature design rules for structural components in nuclear reactors, has developed strength reduction factors for qualified alloys. These reduction factors, which compare a material's strength after aging at a specific temperature and time to the ASME code design strength, are crucial for ensuring the safe design and longevity of structural components, particularly in environments where material degradation is time-dependent.

Providing reliable thermal strength reduction factors for 60 years and beyond, while attempting to shorten the usually lengthy qualification process under the ASME BPV code, requires high-fidelity models of microstructural evolution based on available data from short- to mid-term experiments. Li et al. [7] pioneered this approach by performing microstructural characterization and tension testing on a substantial number of Grade 91 specimens aged up to 18 years, and using the results in developing a microstructure-informed model that predicted the strength evolution to 1×10^6 hours (114 years). This model is currently being employed by the ASME to establish strength reduction factors for G91 steel with a design life of 60 years, highlighting its effectiveness.

While microstructure and property data are often available in the literature for aged conventional alloys, the thermal aging behavior of additively manufactured (AM) alloys remains largely unexplored, leading to uncertainties in their adoption for high-temperature applications. In alloys manufactured by laser powder bed fusion (LPBF), microstructural features generated from the rapid heating and cooling processes include dislocation cell structures, chemical segregation on the cell boundaries (CBs) and grain boundaries (GBs), oxide inclusions, pores, irregular grain morphology, and grain texture. These unique features increase the stored energy in the material and lead to the expectation of reduced thermal stabilities of LPBF alloys, compared to their conventional counterparts, facilitated by dislocation recovery, element redistribution, and precipitation. The impact of such accelerated aging on mechanical properties is expected to be profound.

This section focuses on an as-printed 316H SS manufactured by LPBF and the effect of aging at 550-750°C on its microstructural evolution. For wrought 316H SS, although prolonged thermal aging at the temperature range of 538 to 816°C leads to the decomposition of matrix material through precipitation of $M_{23}C_6$ (M = Cr, Mo, Fe), Laves, sigma, and other phases at grain boundaries, twin boundaries, and dislocations [8], studies have shown that both the yield strength (YS) and the ultimate tensile strength (UTS) values for the aged materials tested at the aging temperatures generally fall above the minimum property curves for the unaged materials, while thermal aging mainly impacts fracture toughness, tensile ductility, and the minimum creep rate [9,10]. For those reasons, the ASME BPV Code Section III, Division 5 specifies a YS reduction factor of 1 (no reduction) and a UTS reduction factor of 0.8 (a 20% reduction) for wrought 316H SS at elevated temperatures (≥480°C) for services up to 60 years.

In this section, the thermal aging experiment of the LPBF 316H SS was performed at 550-750°C for up to 10,000 h (1.14 y). Electron microscopy and high-energy synchrotron X-ray diffraction were used to quantify the dislocation recovery kinetics as well as the fraction and size evolutions

of $M_{23}C_6$, Laves, sigma, and oxide phases. The results showed a 10-100× acceleration of precipitation in the LPBF material compared to its wrought counterpart and were used to construct, for the first time, a time-temperature-precipitation (TTP) diagram for an LPBF material. Uniaxial tension tests were performed at the aging temperatures to reveal the impact of aging on tensile properties. Using experimental data as inputs, a physics-informed model was fit to track the $M_{23}C_6$ and Laves precipitate evolution to 1×10^6 h (114 y), which was then used to extrapolate strength as well as strength reduction factors to such a long term. This physics-informed model incorporates the actual physical mechanisms controlling material strength under thermal aging and should therefore be more accurate compared to curve fitting approaches like the Hollomon–Jaffe method [11], particularly for long aging times. It was shown that the LPBF material experienced a faster decline in tensile strength than the wrought material when compared to their respective initial strengths. However, even after 114 years of simulated aging, the LPBF material retained significantly higher strength than the wrought material. Overall, this study demonstrates a methodology for assessing a material's long-term strength in high-temperature environments based on short- to intermediate-term experiments and paves the way for the rapid qualification and adoption of new materials in energy applications.

3.2 Microstructure

3.2.1 SEM observations

Figure 5 compiles the SEM BSE images of aged LPBF 316H samples in time series. Under all aging conditions the grain structures and the grain sizes do not change. At 550°C, it is seen that, to the resolution of the SEM, fine Mo-Si rich precipitates are observable on grain boundaries (GBs) after 2500 h of aging and on both GBs and CBs after 10000 h of aging. Cr carbides form on those boundaries starting at around 500 h as observed in SE images (not shown). In all aging conditions, round, dark particles of 10 to 200 nm exist preferably on CBs. Those particles are Mn-Si rich oxides known as $MnSiO_3$ Rhodonite, which is formed during the printing process [12].

At 650°C, bright precipitates are present on GBs after 100 h of aging and on both GBs and CBs after 500 h of aging. Those on GBs are larger than those on CBs. Cr carbides are present in the samples after 5 h of aging, observed in SE images (not shown). At 10000 h, a new phase with a light grey contrast is observed (pointed by a black arrow). The large size of the precipitate indicates that it grows rapidly once formed. The dark oxides are present in all conditions and their sizes do not seem to change.

At 750°C, the large light grey phase is the most prominent feature seen on GBs at low magnifications at 500 h and beyond. They can reach 20 μm in size. In addition, smaller bright precipitates are observable on GBs after 5 h of aging and are present on GBs and CBs after 25 h of aging. Carbides are present in samples with as early as 5 h of aging, observed in SE images (not shown).

In comparison, Figure 6 shows the WT 316H samples annealed to 10000 h at 550, 650 and 750°C in low (a-c) and high (d-f) magnifications. Under 550°C and 10000 h, the WT sample only has fine carbides on GBs. Under 650°C and 10000 h, the WT sample has carbides and Mo-Si rich precipitates on GBs, twin boundaries (TBs) and also within grains, but their densities are much lower and the sizes are a bit larger compared to the LPBF sample. No phase with grey contrast is observed. Under 750°C and 10000 h, the WT sample has larger carbides and Mo-Si rich precipitates compared to the 650°C-10000h sample. The grey phase appears, indicated by arrows in Figure 6 (c) and (f).

While in this section we only differentiate the different phases by imaging contrast, in the following sections, we quantify their chemical compositions and the crystal structures with STEM-EDS and high-energy x-ray diffraction, from which they are identified: the bright precipitates are the Laves phase, the large grey phase is the sigma phase, and the carbide is $M_{23}C_6$. The SEM observations of precipitation are thus summarized in Table 4. The phase fractions, measured by the Trainable Weka Segmentation plugin in Fiji, will be presented in Section 3.2.3 along with the measurements from XRD. The particle sizes will be presented in Section 3.4.1 when discussing the effect of thermal aging on tensile strength.

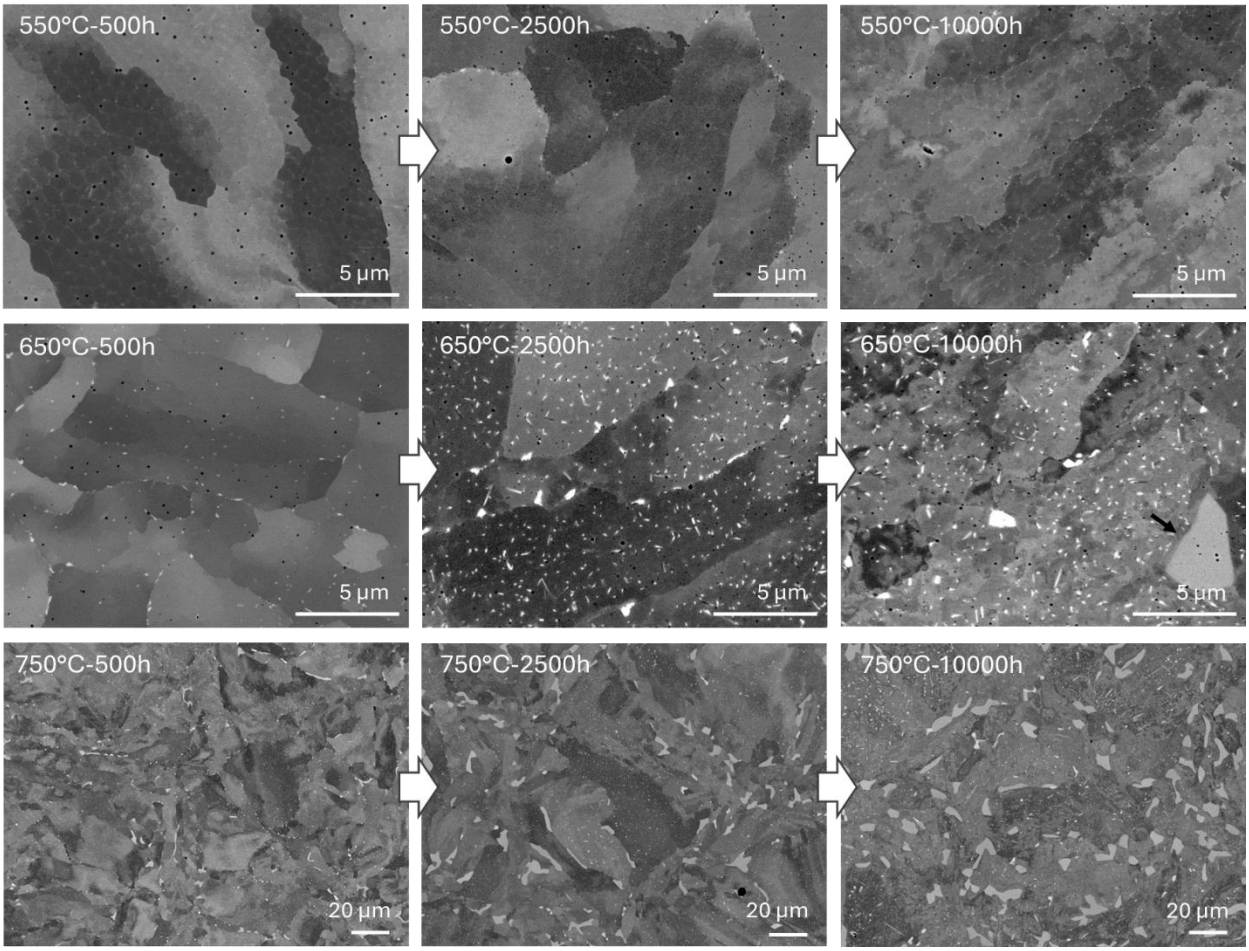

Figure 5. SEM-BSE images of LPBF 316H SS specimens aged at 550, 650 and 750°C for 500, 2500 and 10,000 h.

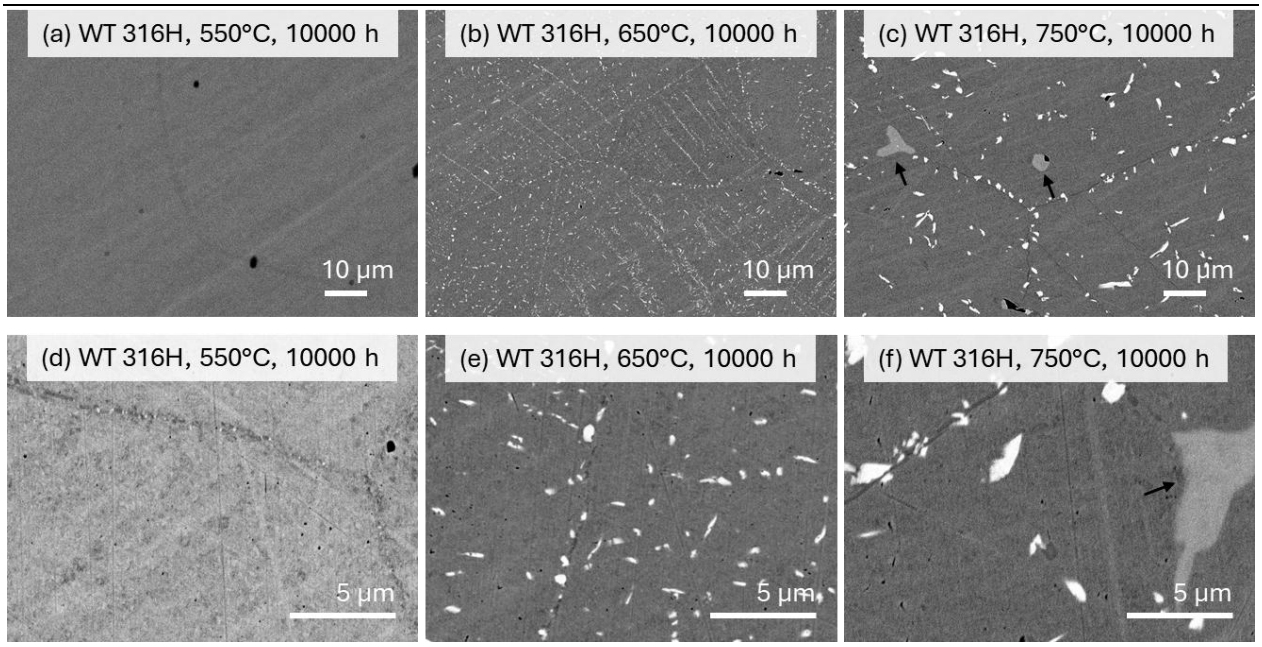

Figure 6. SEM-BSE images of WT 316H SS specimens aged at 550, 650 and 750°C for 10,000 h: (a-c) low magnification images; (d-f) high magnification images.

Table 4. Summary of the SEM observations of precipitation in LPBF 316H and WT 316H specimens.

Aging Time (h)	**550C**	**650C**	**750C**
5 (LPBF)	n/a	$M_{23}C_6$	$M_{23}C_6$ Laves
25 (LPBF)	n/a	$M_{23}C_6$	$M_{23}C_6$ Laves
100 (LPBF)	n/a	$M_{23}C_6$ Laves	$M_{23}C_6$ Laves
500 (LPBF)	$M_{23}C_6$	$M_{23}C_6$ Laves	$M_{23}C_6$ Laves Sigma
2500 (LPBF)	$M_{23}C_6$ Laves	$M_{23}C_6$ Laves	$M_{23}C_6$ Laves Sigma
10000 (LPBF)	$M_{23}C_6$ Laves	$M_{23}C_6$ Laves Sigma	$M_{23}C_6$ Laves Sigma
10000 (WT)	$M_{23}C_6$	$M_{23}C_6$ Laves	$M_{23}C_6$ Laves Sigma

3.2.2 TEM study of 2500-h aged samples

The as-built specimen and the specimens aged at 550, 650 and 750°C for 2500 hours were studied by STEM and EDS. Figure 7 (a-b) presents an EDS line scan across two CBs in the as-built specimen, which shows about 1% of Cr and about 0.8% of Mo enrichment at those boundaries. Figure 7 (c-f) show the STEM-BF images of 2500-h aged samples and the corresponding EDS maps of Cr and Mo. The maps of other elements, including Fe, Ni, Mn, O, C, and Si are included in the Supplementary Information. Figure 7 (c) shows a STEM-BF image and the corresponding EDS maps of Cr and Mo around a dislocation cell in the 550°C-2500h specimen. 5-25 nm sized precipitates enriched in Cr are formed on the CB, as pointed by the magenta arrows in the Cr map. They are likely Cr carbides. In addition, Mo-Si rich precipitates of about 50 nm, as pointed by the green arrows in the Mo map, are also formed. An oxide particle is in the view, as pointed by the white arrow in the STEM image.

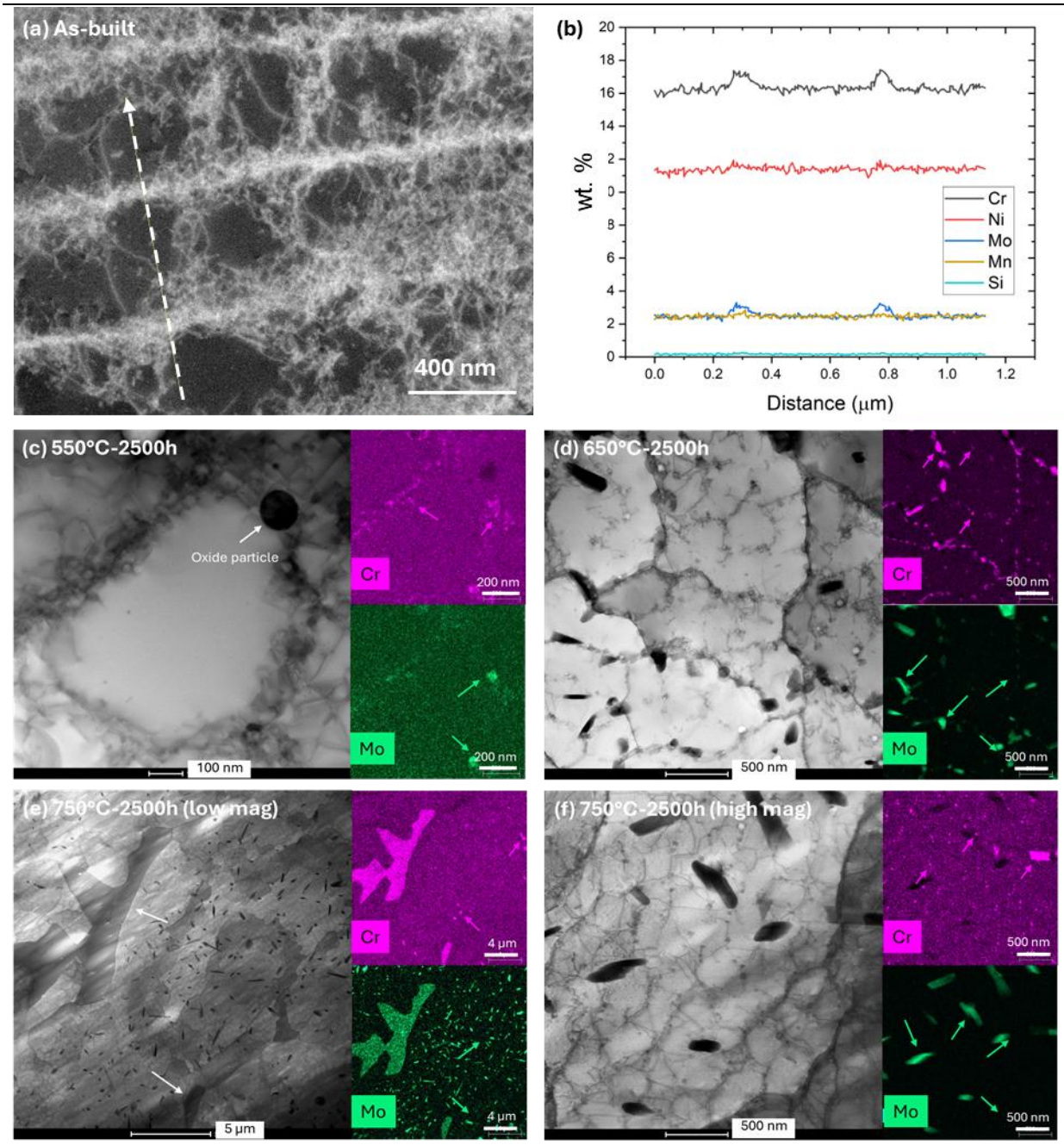

Figure 7. (a) A STEM-HAADF image of the as-built LPBF 316H specimen with the dashed line showing the EDS line scan path. (b) The concentration of selected elements along the EDS scan path in (a). (c) A STEM-BF image of the 550°C-2500h aged LPBF 316H specimen along with the corresponding EDS maps of Cr and Mo. (d) A STEM-BF image of the 650°C-2500h aged LPBF 316H specimen along with the corresponding EDS maps of Cr and Mo. (e, f) STEM-BF images at low (e) and high (f) magnifications of the 750°C-2500h aged LPBF 316H specimen along with their corresponding EDS maps of Cr and Mo. For the EDS maps, the image contrast has been tuned for better visibility of small precipitates with brighter areas indicate higher concentrations and vice versa.

Figure 7 (d) shows a STEM-BF image and the corresponding EDS maps of Cr and Mo in the 650°C-2500h specimen. While the cell structure still remains, the CBs are much thinner. Mo-Si rich precipitates, smaller than 1 μm in length, are formed extensively within the grains and on HAGBs (see Supplementary Information). Within the grains, they are associated with CBs and LAGBs, as pointed by the green arrows in the Mo map. Similarly, Cr carbides form on CBs, LAGBs, and HAGBs, as pointed by the magenta arrows in the Cr map. The sizes of Cr carbides are generally smaller than those of the Mo-Si rich precipitates.

Figure 7 (e-f) shows two STEM-BF images and their corresponding EDS maps of Cr and Mo in the 750°C-2500h specimen. The CBs are just a few dislocations in most cases. On the CBs, Cr carbides are observed with an average size of 30 nm, as pointed by the magenta arrows in the Cr map. Also associated with CBs are Mo-Si rich precipitates that are a few hundreds of nm to 1 μm in length, as pointed by the green arrows in the Mo map. On GBs, very large Mo-Cr rich precipitates spanning 5-20 μm are formed, as pointed by the white arrows in Figure 7 (e) in the STEM image.

Quantitative EDS analysis shows that the Cr carbide has a composition of 63.1Cr-20.0Fe-10.5Mo-3.1Ni-1.1Mn (values in wt.%). Due to the inability of STEM-EDS in accurately quantifying low-Z atoms such as C and O, those two elements are not reported here. This composition is in good agreement with literature reports of $M_{23}C_6$ in 316 SS, for example, see Weiss *et al*. [13]. The Mo-Si rich phase has a composition of 44.3Fe-34.2Mo-13.9Cr-5.7Ni-1.9Si (values in wt.%), which is in reasonably good agreement with that of the Laves phase found in aged 316 stainless steel [14]. The large Mo-Cr rich phase has a chemical composition of 50.8Fe-32.6Cr-9.6Mo-5.2Ni-0.86Mn-0.55Si-0.46O (values in wt.%), in reasonably good agreement with the composition of the sigma phase found in aged 316 stainless steel [14–16] except for the existence of the small amount of oxygen, likely as an interstitial element.

3.2.3 High-energy synchrotron x-ray diffraction

High-energy synchrotron x-ray diffraction measurements were performed on the unaged (as-built) and aged LPBF 316H specimens to determine the phase types and the phase fractions. Figure 8 (a) shows the raw detector images (cropped from the original size) of the unaged and some 650°C aged specimens in increasing aging times. The unaged specimen only has diffraction rings from the austenite matrix phase. As the aging time increases, diffraction signals from secondary phases emerge. At 100 h, rings from the $M_{23}C_6$ phase are clearly observed. At 2500 h, additional rings from the Laves phase are observed. At 10000 h, spots from the sigma phase are populated, indicating that the crystallite size of this phase is large.

Figure 8 (b-d) plot the line profiles of the unaged and aged LPBF 316H specimens at 550, 650 and 750°C, respectively, magnified to highlight the secondary phase peaks. Some major secondary peaks are labeled: “C”, “L”, and “S” stand for $M_{23}C_6$ carbide, Laves phase, and sigma phase, respectively. GSAS-II was able to deconvolute the peak profiles and provided the phase volume fractions for each specimen. Figure 9 plots the phase fractions as a function of aging time under different temperatures; values obtained from XRD and SEM are all included. While XRD provides volume fractions and SEM provides areal fractions, assuming the material is isotropic and the distribution of the precipitates is uniform in all directions, the areal fraction can approximate the volume fraction statistically, known as the stereological principle [17]. Looking at just the XRD results (solid symbols with solid lines), it is seen that at 550°C, $M_{23}C_6$ carbide becomes measurable upon 500 h of aging and is the only detectable secondary phase. At 650°C, $M_{23}C_6$ carbide, the

Laves phase, and the sigma phase become measurable at 5, 500 and 10000 h, respectively. Unlike the slow precipitation of the Laves phase and $M_{23}C_6$, the sigma phase emerges in a drastic way and has reached to a volume fraction of 4.7% upon its first detection at 10000 h. At 750°C, $M_{23}C_6$ carbide, the Laves phase, and the sigma phase become measurable at 5, 25 and 500 h, respectively. On the other hand, SEM results in Figure 9 (open symbols with solid lines) show that the Laves phase is more prevalent at all aging conditions than what is detected under XRD. A plausible explanation is the overlap of a major peak of the Laves phase at ~2.36 Å with one from the $M_{23}C_6$ carbide at ~2.38 Å, along with other overlaps, makes the peak profile analysis less accurate.

In comparison to those in the LPBF 316H material, the Laves and the sigma phase fractions from the 500-h and longer aged WT 316H are also plotted in Figure 9 (SEM measurements; half-open symbols with dashed lines). It is seen that while the Laves phase in the WT material can be as prevalent as that in the LPBF material during longer-term aging at 650 and 750°C, the sigma phase is significantly suppressed. $M_{23}C_6$ carbide is not readily measurable from SEM images due to the poor contrast as described previously, so it is not quantified for the WT material.

Figure 9 also plots the oxide fraction evolution in the LPBF 316H material as measured from SEM images. The oxide is not detected in XRD, due to the fact that this phase is amorphous [18]. Nevertheless, the results show that the oxide phase fraction remains relatively stable under all aging conditions.

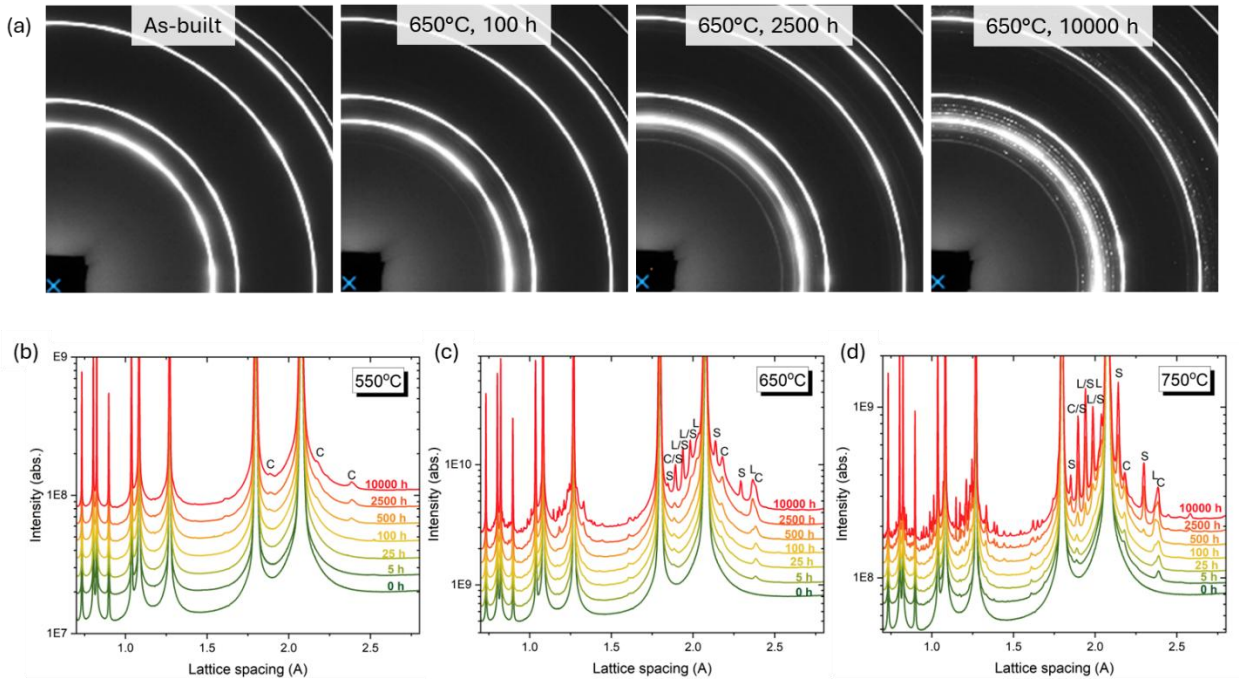

Figure 8. (a) Series of X-ray detector images of the unaged (as-built) and some 650°C aged specimens with increasing aging times. The images were cropped from their original size, which contains the full azimuthal range, to enhance the view of signals emerged with aging. (b-d) X-ray line profiles of specimens aged at 550, 650, and 750°C, respectively, enlarged and offsetted for better view of the evolution of minor phase peaks as a function of aging time.

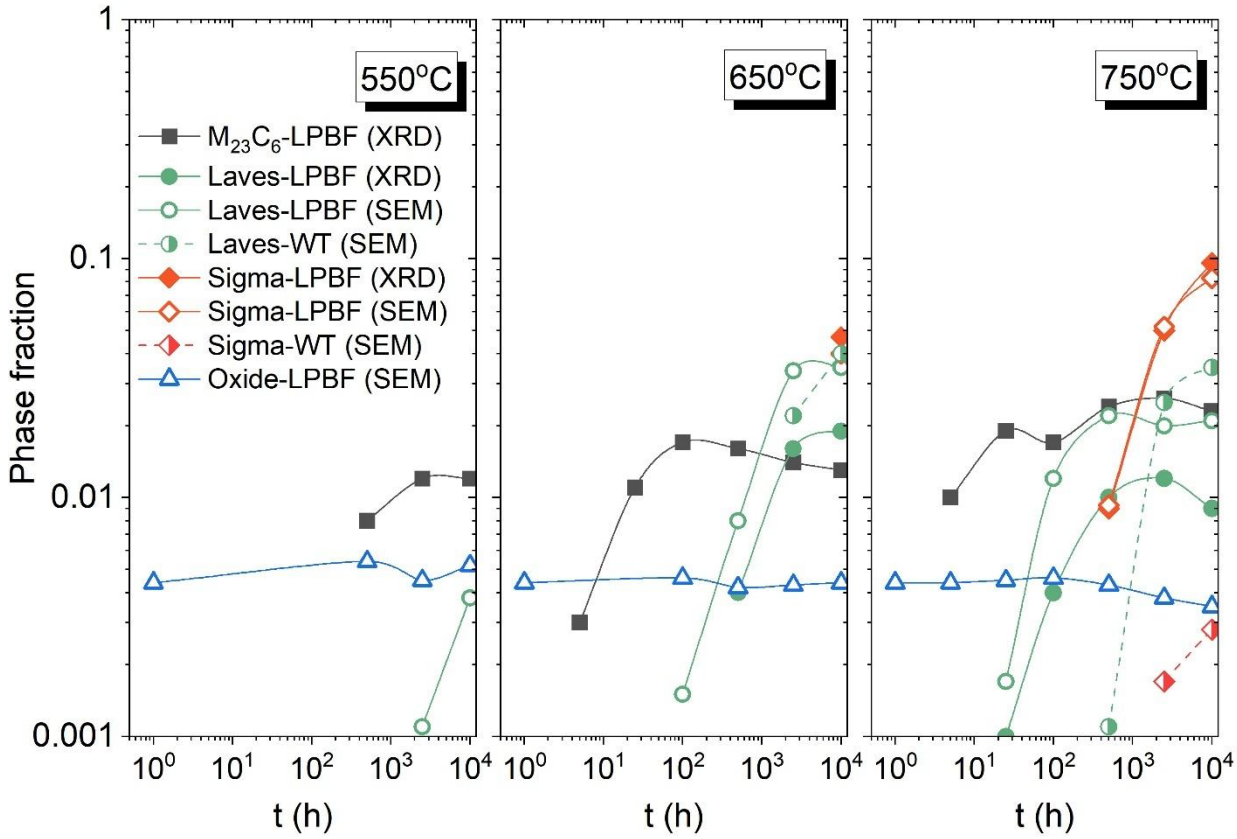

Figure 9. Volume fractions of secondary phases as a function of aging time in LPBF and WT 316H specimens aged at 550, 650, and 750°C (left to right). For the LPBF 316H specimens, values were obtained from XRD (solid symbols) and SEM (open symbols) measurements. For the WT 316H specimens, values were obtained from SEM measurements (half-filled symbols).

Figure 10 summarizes the observed phases in SEM at different aging conditions. Based on those observations, the TTP diagram for LPBF 316H SS is determined. The solid lines in Figure 10 are from this study while the dashed lines are adopted from Ref. [19] for WT 316H SS developed by the National Institute for Materials Science, Tsukuba, Japan. The precipitation of Laves and sigma phases in WT 316H, as predicted by the dashed lines, is in good agreement with our experimental observation shown in Figure 9 (half-open symbols). Compared to WT 316H, LPBF 316H shows an acceleration of precipitation by 10-100 times. The high density of dislocations, LAGBs, and CBs in the as-printed LPBF material serve as preferred nucleation sites and rapid diffusion paths. These, together with the Cr and Mo segregation on LAGBs and CBs to lower the nucleation barrier, are the main contributors to the accelerated precipitation, in a way similar to the effect of cold work on conventional materials [16].

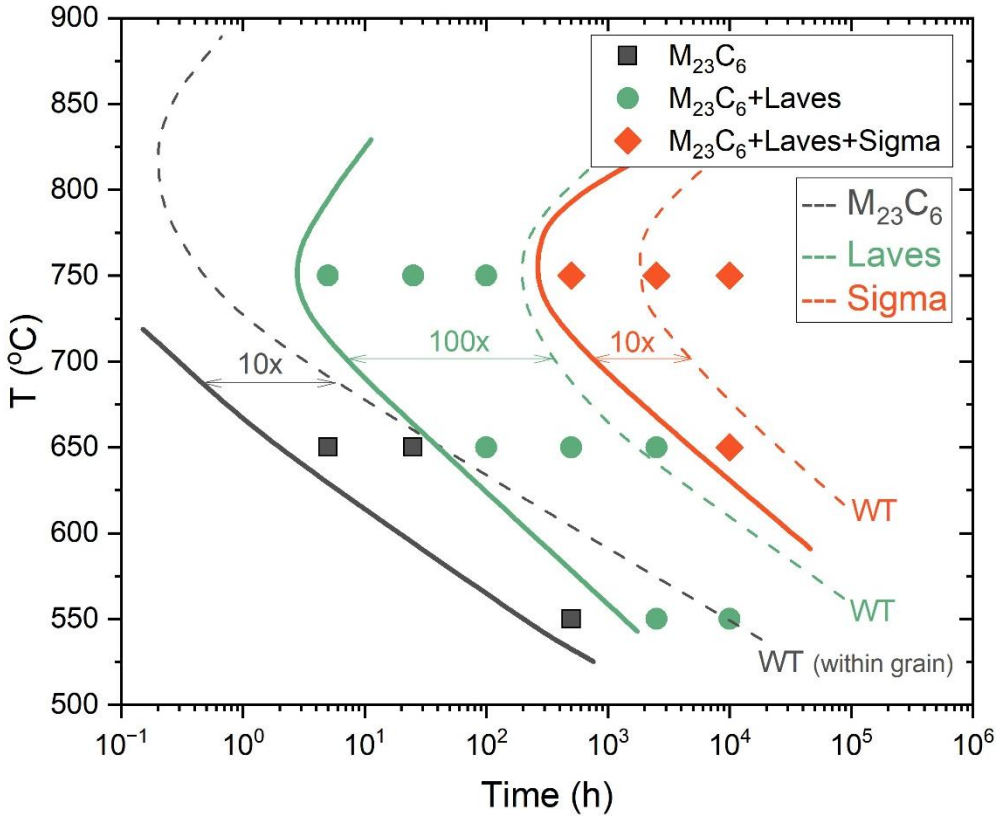

Figure 10. The time-temperature-phase (TTP) diagram for LPBF 316H SS (solid lines) based on experimental observations (symbols), overlapped with the TTP diagram for WT 316H SS (dashed lines) from the National Institute for Materials Science (Tsukuba, Japan) [19].

3.3 Tensile properties

The evolution of microstructures during thermal aging has a profound effect on the tensile performance of LPBF 316H SS. Figure 11 shows the tensile curves of unaged and aged LPBF materials tested at aging temperatures. The vertical specimens are in separate groups from the horizontal specimens for better visualization. The curves from the as-received and the 10000h-aged WT material are also included for comparison purposes. The materials in general have strong dynamic strain aging (DSA) when tested at 550°C, which becomes weaker at 650°C and disappears at 750°C. At 550°C, DSA persists in all materials aged to 10,000 h. At 650°C, DSA is prominent in the 500-h or shorter aged material but disappears in the 2,500-h and 10,000-h aged materials , as seen in Figure 11 (b) magnified view, as the solutes that hinder the dislocation motion get immobilized into precipitates.

The anisotropy in tensile strength between the vertical ("V") and the horizontal ("H") specimens is observed in Figure 11. The H specimens in general have higher yield strength (YS) and ultimate tensile strength (UTS) than the V specimens, in agreement with literature reports [20]. While an explanation for the anisotropy is not pursued in this research, literature has shown that the grain texture provides the dominant contribution [20,21].

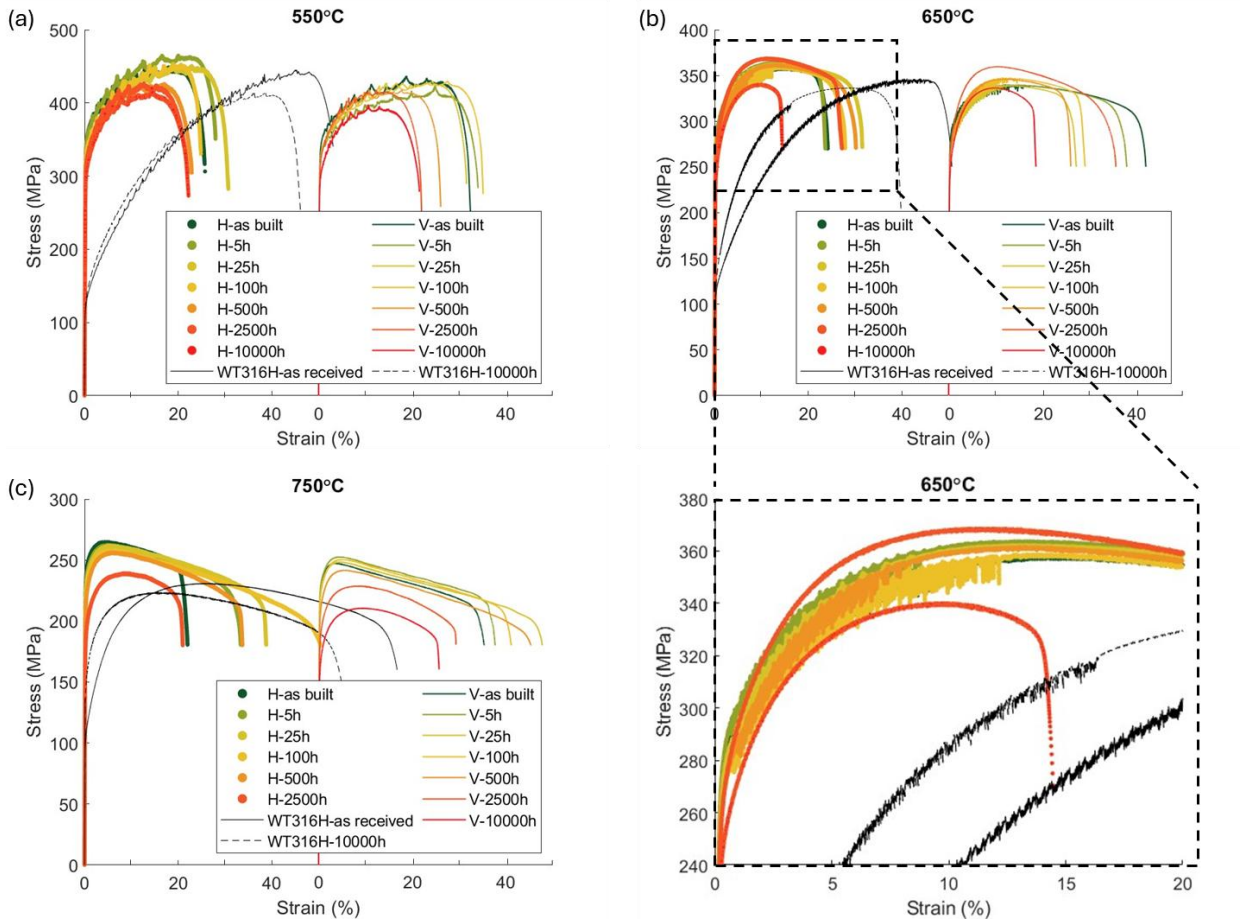

Figure 11. Tensile curves of aged LPBF 316H specimens tested at their aging temperatures: (a) 550°C; (b) 650°C; (c) 750°C. Note the differences in the range of the vertical axis. The curves from unaged and 10000h-aged WT 316H specimens are included for comparison purposes. The curves for vertical specimens are shifted along the strain axis on each graph for better visualization.

Figure 12 plots the values of YS, UTS, uniform elongation (UEL), and total elongation (TEL) of LPBF and WT 316H specimens as a function of aging time. The LPBF specimens are shown in a line+symbol format, with open symbols for the vertical (V) specimens and solid symbols for the horizontal (H) specimens, while the WT specimens are shown in a dotted line format. The temperature color code is consistent between the LPBF and the WT specimens.

For the LPBF material, Figure 12 shows that aging and testing at 550°C, the material shows a slow decrease in YS and UTS but a relatively quick decrease in UEL and TEL past 25 h of aging. Aging and testing at 650°C, the material's strength and ductility remain relatively stable until 2500 h of aging, after which they start to decrease. Aging and testing at 750°C, the material shows a relatively quick decrease in YS and UTS but an increase in UEL. The TEL values of all specimens have large scatter but a general reduction trend towards long aging times can be speculated.

For the WT material, Figure 12 shows that aging does not degrade the material's YS; instead, the YS at all temperatures increases moderately with aging time, in agreement with literature reports [9,10], which can be understood by precipitation hardening. The UTS of the WT material shows a

moderate decrease while the UEL shows a quicker decrease at all temperatures. The TEL shows a general decreasing trend as well.

The obvious aging-induced reduction in YS of the LPBF material may raise safety concerns during prolonged services at high temperatures. In Section 3.4, we will correlate the microstructural evolution with the YS changes and predict the YS to 1×10^6 h (114 y).

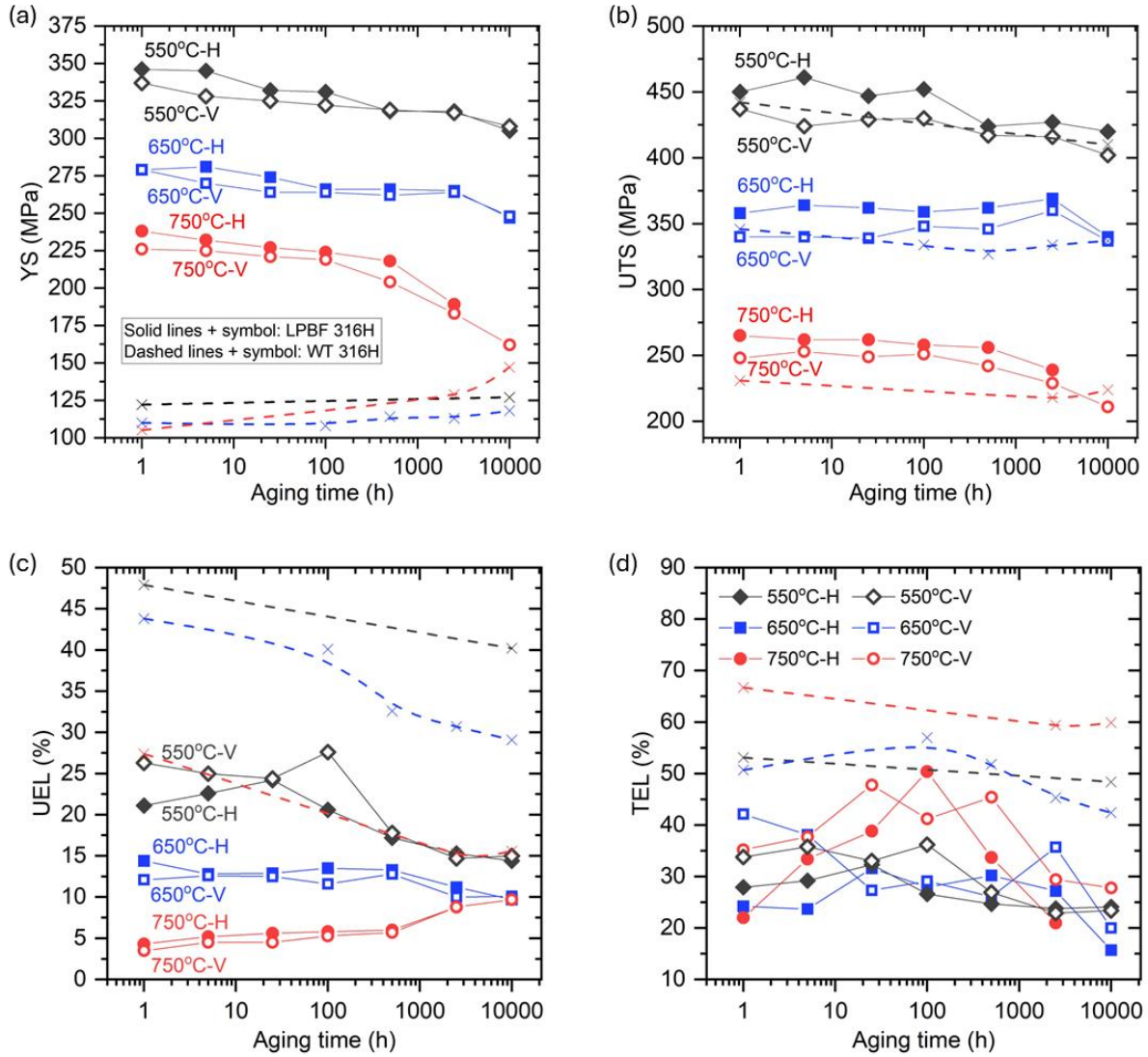

Figure 12. (a) Yield strength (YS) of the LPBF and the WT materials as a function of aging time. (b) Ultimate tensile strength (UTS) of the LPBF and the WT materials as a function of aging time. (c) Uniform elongation (UEL) of the LPBF and the WT materials as a function of aging time. (d) Total elongation of the LPBF and the WT materials as a function of aging time. All tests were performed at the aging temperatures. The LPBF material is shown in a line+symbol format, with open symbols for the vertical (V) specimens and solid symbols for the horizontal (H) specimens, while the WT material is shown in a dotted line format. The temperature color code is consistent between the LPBF and the WT materials.

3.4 Precipitation model, strengthening model, and long-term prediction

3.4.1 Precipitation model

We developed a model for precipitation in 316H to extend the experimental data in time and predict the long-term evolution of precipitates in the material. The model resembles the precipitation model developed for wrought 316H by Hu et al. [22], with modifications described in Reference [23]. The main modification in Reference [23] is that the precipitates can compete for elements in the solid solution, unlike the original model [22] where each precipitation reaction was independent from the others.

The model tracks the number density (N) and mean radius (r) of each phase, which can be converted to diameter and volume fraction to match the experimental data presented in this work. The model represents the nucleation, growth, and coarsening of precipitates following classical mean-size nucleation and growth [24] and coarsening [25] kinetics, specifically:

$$\dot{N}_{i,growth} = N_{0,i}\frac{2V_{m,i}D_i\tilde{c}_{i,j}}{N_a a_m^4}\sqrt{\frac{\chi_i}{kT}}\exp\left(\frac{16\pi\chi_i^3}{3G_i^2}\right) \quad (1)$$

$$\dot{N}_{i,ripening} = \frac{-3N_i}{r_i\dot{r}_{i,ripening}} \quad (2)$$

$$\dot{r}_{i,growth} = \frac{D_i}{r_i}\frac{\tilde{c}_{i,j}-\tilde{c}_{i,j,eq}}{\tilde{c}_{i,j,p}-\tilde{c}_{i,j,eq}} - \frac{\dot{N}_{i,growth}}{N_i}\left(\frac{2\chi_i}{G_i}+r_i\right) \quad (3)$$

$$\dot{r}_{i,ripening} = \frac{8\chi_i V_{m,i}D_i\tilde{c}_{i,j}}{9RT}\frac{1}{3r_i^2} \quad (4)$$

In these equations subscript i represents a precipitate type and j represents an element in the precipitate and in the solid solution. c represents concentration as a mass fraction. The notation $\tilde{c}_{i,j}$ represents the concentration of the element in the solid solution j limiting the rate of growth of the precipitate i (typically the slowest diffusing species). For concentrations a subscript c_{eq} represents the equilibrium concentration of that element in the matrix and c_p the (equilibrium) concentration in the precipitate. Unsubscripted concentrations are the current concentration in the matrix. N_0 is a reference nucleation rate, D the controlling diffusivity, and χ the surface energy of each precipitate. G_i is the Gibbs energy driving the reaction, calculated assuming competition amongst precipitates for free elements in solution. The implementation of the model has a soft switch via a sigmoid function between the growth and ripening regimes as a function of the difference in current concentration in the matrix and the equilibrium concentration in the matrix of each species participating in each reaction.

The remaining values are the absolute temperature T, physical data about the precipitate and matrix phases (molar volume V_m and lattice spacing of the matrix a_m), or physical constants (Avogadro's number N_a, Boltzmann constant k, and universal gas constant R).

The model tracks the evolution of the $M_{23}C_6$ carbide, Laves, and sigma phases. The model couples the evolution of the Laves and carbide phases but treats the sigma phase separately. For each aging temperature we fit the controlling diffusivity and the reference nucleation rate for each precipitate to the short-term experimental data and used the model to extrapolate the behavior to longer aging times.

We adopt literature values for the physical parameters in the model, including the composition, molar volume, and surface energy of each precipitate and the lattice parameter of the matrix [22]. The model tracks the diffusion and reaction of Cr, C, and Mo in the material. Thermo-Calc simulations with the TCFE13 database establish the equilibrium chemistry of the matrix for each aging temperature. For these simulations we suppressed the formulation of delta ferrite to match the experimental determination of an essentially ferrite-free matrix, reflecting the rapid cooling rate in the LPBF process. For the precipitation calculations we increased the amount of free C in the matrix from the Thermo-Calc results by a fraction of the experimentally-measured O, reflecting the potential for oxygen to participate in the formation of carbides in AM material with higher-than-typical oxygen content compared to wrought material.

3.4.2 Strengthening model

The continuous reduction in the tensile yield strength during aging of the LPBF 316H material is contradictory to the behavior of WT 316H materials, which is either unaffected or increased by aging, as shown in our results in Figure 12 as well as in literature reports [9,10]. To understand this, we consider the following microstructural processes during aging of LPBF 316H that have impacts on material's strength: dislocation recovery, evolution of carbide, Laves, sigma and oxide phases, and depletion of Mo solutes. Note that the dislocation cell evolution is the same process as the dislocation recovery and therefore it is not included as a standalone process.

3.4.2.1 Dislocation recovery

The dislocation recovery is facilitated by the annihilation of dislocation dipoles via thermally activated climb [26,27]. The recovery rate is often described by an Arrhenius-type equation:

$$\frac{\mathrm{d}\rho}{\mathrm{d}t} = -K\rho^n e^{-\frac{Q}{RT}} \tag{5}$$

where ρ is the dislocation density, t is time, K is a material-dependent constant, n is an empirical constant, Q is the activation energy for recovery, R is the universal gas constant (8.314 J/mol/K), and T is the absolute temperature. As n is often greater than 1, the integration of the equation above gives:

$$\rho(t) = \left[\rho_0^{1-n} - (1-n)Ke^{-\frac{Q}{RT}}t\right]^{\frac{1}{1-n}} \tag{6}$$

which can be rearranged into:

$$\begin{aligned}\ln\rho(t) &= \frac{1}{1-n}\ln\left[\rho_0^{1-n} - (1-n)Ke^{-\frac{Q}{RT}}t\right] \\ &= \frac{1}{1-n}\left[\ln\left((n-1)Ke^{-\frac{Q}{RT}}\right) + \ln\left(t + \frac{\rho_0^{1-n}}{(n-1)Ke^{-\frac{Q}{RT}}}\right)\right]\end{aligned} \tag{7}$$

The dislocation recovery process at 550, 650, and 750°C for 1 h in a LPBF 316H sample has been characterized via *in-situ* high-energy synchrotron XRD. Figure 13 (a) shows the measured dislocation density as a function of annealing time at each temperature. The fitting to the data according to Equation (7) is shown on top of the experimental data in white lines. The fitting yields $\ln\rho = 33.97 - 0.11\ln(t+10)$ at 750°C, $\ln\rho = 34.40 - 0.11\ln(t+161)$ at 650°C, and

$\ln \rho = 35.04 - 0.11 \ln(t + 18647)$ at 550°C. Accordingly, it can be deduced that $n = 10.1$, $Q = 320$ kJ/mol/K, $\ln K = -279$, and $\rho_0 = 6.3 \times 10^{14}/\mathrm{m}^2$.

The dislocation recovery equations are used to calculate the dislocation density of the materials after aging. Figure 13 (b) plots the dislocation density as a function of aging time at 550, 650, and 750°C. Those values are used to calculate the dislocation hardening, following:

$$\triangle \sigma_{\mathrm{d}} = M\alpha Gb\rho^{0.5} \tag{8}$$

where *M*, *G*, and *b* represent the Taylor factor (3.06 for FCC material), the shear modulus (61 GPa at 550°C, 58 GPa at 650°C, and 53 GPa at 750°C), and the Burgers vector value (0.258 nm at 550°C, 0.259 nm at 650°C and 750°C), respectively. The parameter α corresponds to the barrier strength of dislocations which is typically around 0.2 for austentitic SS [28,29].

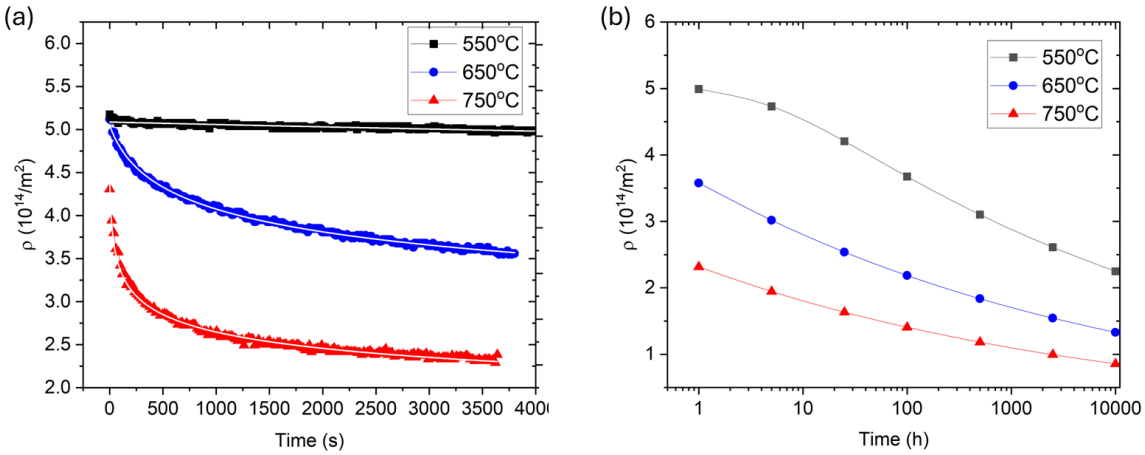

Figure 13. (a) The dislocation density of LPBF 316H SS as a function of annealing time at 750°C (in-situ XRD measurements and fitting). (b) The dislocation density of LPBF 316H SS as function of aging time at 550, 650, and 750°C (calculated).

3.4.2.2 $M_{23}C_6$, Laves, sigma, and oxide phase evolution

Figure 9 shows the volume fraction evolutions of $M_{23}C_6$, Laves, sigma and oxide phases during thermal aging. The data of $M_{23}C_6$ and Laves phases are replotted in Figure 14 (a) and (b), along with the model results up to 1×10^6 h. The average size evolutions of $M_{23}C_6$ and Laves particles are plotted in Figure 14 (c) and (d), including measurements from SEM images and results from modeling. Overall, good agreements between the experiment and the model are achieved. For oxide particles, since they appear to be very stable under all aging conditions, an average size of 80 nm and a constant volume fraction of 0.44% are adopted.

The size and fraction information of the $M_{23}C_6$, Laves, and oxide phases are used in calculating Orowan strengthening, following:

$$\triangle \sigma_i = \frac{0.4MGb}{\pi\sqrt{1-\upsilon}} \frac{\ln \frac{r_i \pi}{2b}}{L_i} \tag{9}$$

where the subscript *i* refers to a given particle species, υ is the Poisson's ration (0.27), r is the mean particle radius, and L is the mean particle spacing, calculated using $L=r \times [(2\pi/3f)^{0.5} - 0.5\pi]$

assuming the particles are randomly distributed spheres with *f* being the measured volume fraction of species *i*.

The consideration of the sigma phase on the material's strength is different. As shown in Figure 9, the sigma phase appears abruptly in LPBF 316H during long term aging at 650 and 750°C. They form at grain junctions and quickly reach μm-level sizes with total volume fractions of a few percent. Those hard, intermetallic particles are considered non-strengthening [9] as their sizes are too big to be effective in pinning dislocations in the matrix.

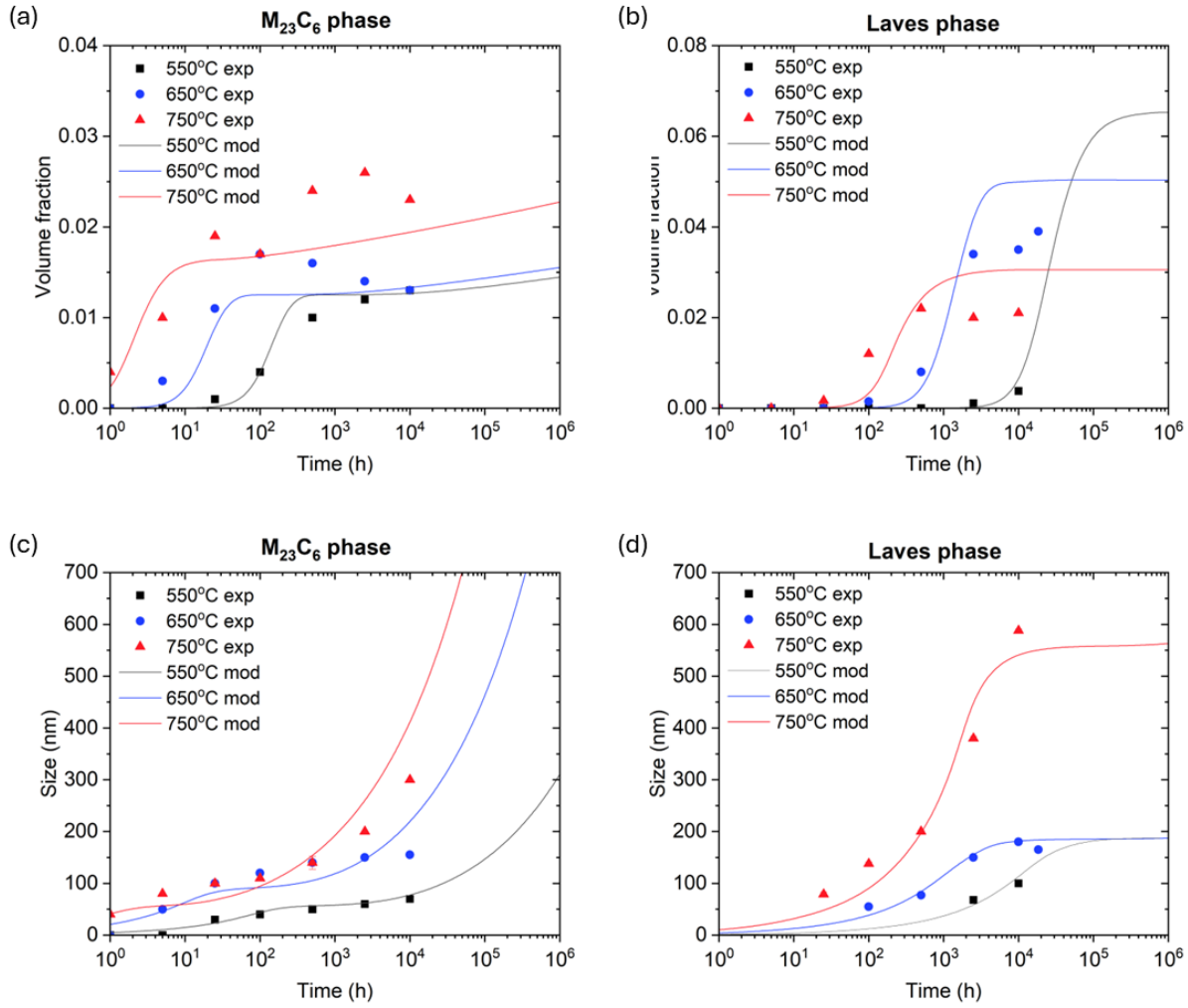

Figure 14. The evolution of $M_{23}C_6$ and Laves precipitates in LPBF 316H SS as a function of time and temperature: (a) volume fraction of $M_{23}C_6$; (b) volume fraction of Laves; (c) size of $M_{23}C_6$; (d) size of Laves. Experimental measurements are shown in connected symbols and modeling results are shown in dashed lines. While the standard deviations of the precipiate sizes range from 50 to 200 nm, due to the large number of preciptates measured (hundreds to thousands), the standard errors of the mean for the average sizes are between 2-5 nm, indistinguishable from the plots.

3.4.2.3 Solute concentration evolution

At room temperature, the contribution of solute atoms to the yield strength of stainless steels has been studied as summarized in Reference [30]. Among the models, linear relationships have been commonly adopted such that the solute contribution to flow strength is proportional to its concentration with a coefficient specific to the solute species. Here we mainly consider Mo solutes, as Mo is the element that sees the most change in wt.% from thermal aging (see Supplementary Information). $\Delta\sigma_{\mathrm{Mo}} = KC_{\mathrm{Mo}}$, with C being the concentration in wt.% and the coefficient K being around 14.6 MPa/wt.% at room temperature [31]. As K is proportional to the shear modulus, which is 77, 61, 58, and 53 GPa at RT, 550, 650, and 750°C, it is calculated to be 11.6, 11.0 and 10.0 MPa/wt.%, respectively, for tests at 550, 650, and 750°C.

The Mo solute concentration in the matrix decreases with aging due to the formation of Mo-rich phases including $M_{23}C_6$, Laves and sigma. Figure 15 (a) plots the change of C_{Mo} with aging time and temperature. The symbols are experimental measurements based on the matrix peak positions measured in XRD. According to Thermo-Calc calculations, the lattice constant of the matrix is inversely proportional to C_{Mo} (Figure 15 (b)), and that is how C_{Mo} was deduced experimentally. In addition to XRD measurements, Figure 15 (a) also has three data points from the STEM-EDS measurements of the 2500-h aged specimens. The dashed lines in Figure 15 (a) are the modeling output. The quicker onset of C_{Mo} reduction observed experimentally, compared to the modeling output, could be caused by other processes that happen during aging, such as stress relaxation. Nevertheless, the results are in reasonable agreement and are used in calculations.

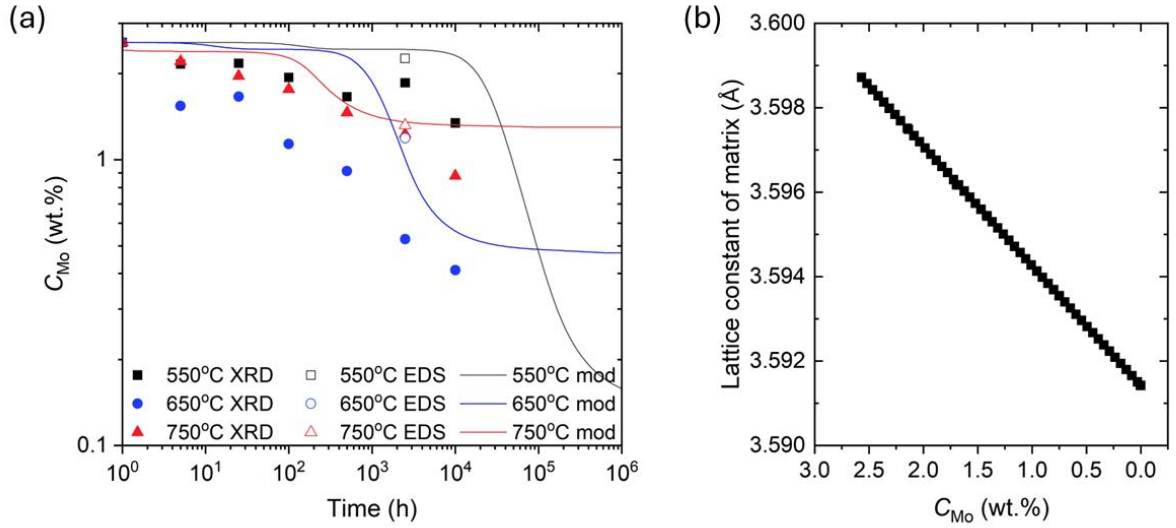

Figure 15. (a) Mo solute concentration in the matrix as a function of aging time and temperature, as determined by XRD measurements, STEM-EDS measurements, and modeling. (b) Lattice constant of the stainless-steel matrix as a function of Mo solute concentration, calculated using ThermoCalc software.

3.4.2.4 Microstructure-strength correlation in aged LPBF 316H

Based on the previous discussions, the yield strength of an aged LPBF 316H material is calculated as follows:

$$\sigma = \sigma_0 + \Delta\sigma_{\mathrm{Mo}} + \sqrt{\triangle\ {\sigma_{\mathrm{d}}}^2 + \sum_i \Delta\sigma_i^2} \quad (10)$$

where σ_0 is a constant contribution and is found to be 106, 92, and 68 MPa, respectively, for 550, 650, and 750°C tests. Those values, which have been tuned to best fit the calculated σ to the experimental data, are based off the ASME Section III, Division 5's design values for yield strength of WT 316H, which are 116, 110, and 94 MPa, respectively, for 550, 650, and 750°C [6]. WT 316H is considered having a clean microstructure so its strength largely reflects the intrinsic strength. The species *i* includes $M_{23}C_6$, Laves, and oxide phases. The quadratic rule of mixtures for calculating the total strength contribution from dislocations and particles is adopted from References [32,33], and the quadratic rule of mixtures for calculating the total strength contributions from different species of particles is adopted from Reference [34]. The calculations in comparison to experimental measurements are shown in Figure 16. The solid lines in Figure 16 (a) show the strength calculated using experimental results for dislocation density, Mo concentration, average precipitate size, and precipitate volume fraction. The agreement between the calculations and the actual YS validates the modeling results for Mo concentration, average precipitate size, and precipitate volume fraction to 1×10^6 h (114 y) in Equation (10) for strength calculation, presented in Figure 16 (b). Figure 16 (c), (d), and (e) show the time-dependent strength contributions from dislocations, $M_{23}C_6$ precipitates, Laves phase precipitates, oxides, and Mo solutes, for 550, 650, and 750°C, respectively. It is concluded that the long-term decay in strength mainly resulted from the dislocation recovery and the coarsening of $M_{23}C_6$ particles. However, even after 114 years of simulated aging, the LPBF material retained significantly higher strength than the wrought material (the ASME Section III, Division 5 design values for YS of wrought 316H are presented as horizontal lines in Figure 16 (a, b)).

As the time is on a logarithmic scale, any validation to the model requires aging to several years or even tens of years. At the time of writing this paper, samples aged to 18,440 h became available and were tested. The data from this longest test was not used to calibrate the model. Their YS values, presented in star symbols in Figure 16 (b), agree very well with the model predictions, validating the effectiveness of this approach in predicting material's long-term aging behavior.

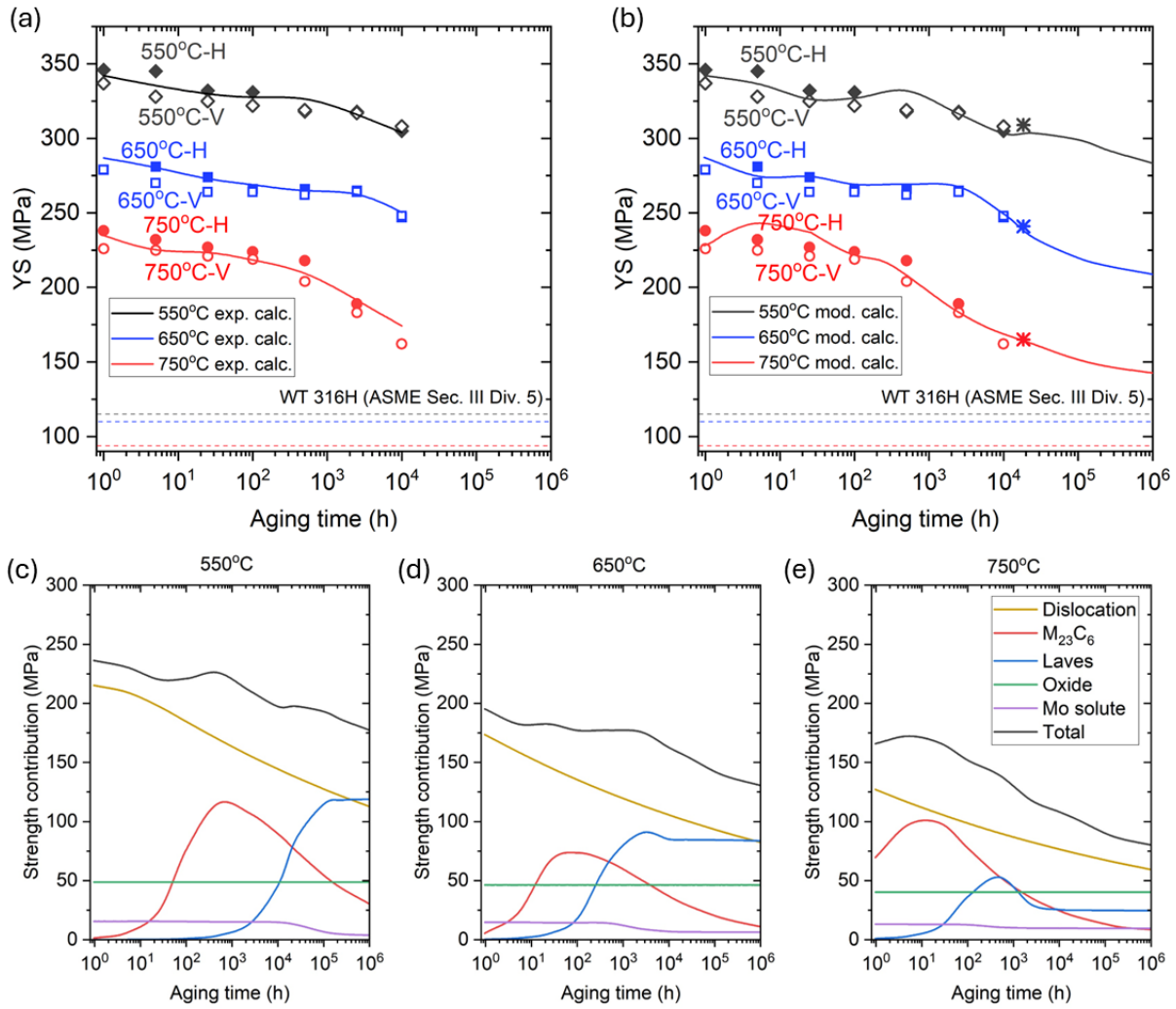

Figure 16. (a) YS of LPBF 316H specimens as a function of aging time to 1×10^4 h. Symbols: experimental measurements; solid lines: calculations using experimental data as input. (b) YS of LPBF 316H specimens as a function of aging time to 1×10^6 h. Symbols: experimental measurements; solid lines: calculations using modeling result as input. The horizontal, dashed lines in (a) and (b) are the ASME Section III, Division 5 design values for YS of wrought 316H, color-coded by temperature in the same way as the LPBF material. (c-e) Time-dependent strength contributions from different microstructural features at 550, 650, and 750°C.

3.4.3 Prediction of long-term strength reduction factors

Figure 17 shows the YS reduction factor up to 1×10^6 h (114 y) for LPBF 316H SS when compared to its initial strength. Aging at all three temperatures resulted in significant strength reduction that becomes more pronounced as the temperature increases. As shown in Figure 16 (c-e), the dislocation recovery and the coarsening of $M_{23}C_6$ precipitates are the major contributors to this strength reduction. Recall that the ASME BPV code Section III, Division 5 specifies that for WT 316H the YS reduction factor is 1 (no reduction) between 480 and 816°C for up to 60 years. The reason for the difference is that, in WT 316H SS, the starting microstructure is "clean" with much

lower density of preferred nucleation sites compared to the LPBF material. Despite the significant strength reduction, as we pointed out in Section 3.4.2.4, LPBF 316H still retains higher strength than WT 316H upon long-term aging, making the strength reduction less concerning.

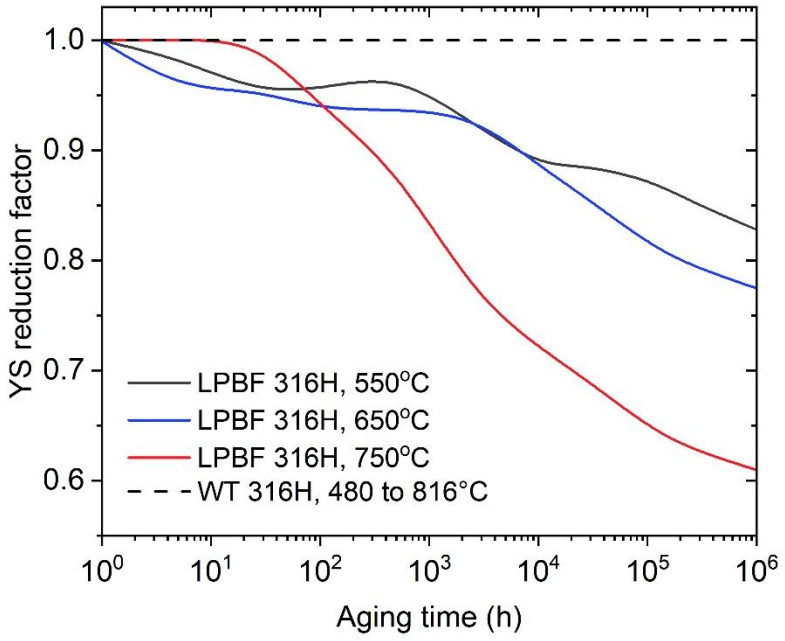

Figure 17. YS reduction factors as a function of time and temperature calculated for LPBF 316H based on the multi-component physics-informed model. ASME BPV code Section III, Division 5's specification regarding WT 316H is also included.

3.5 Conclusions on thermal aging of as-built LPBF 316H

This study provides a comprehensive investigation of the thermal aging behavior and strength degradation of a LPBF 316H SS at 550–750°C. Experimental results for up to 10,000 h (1.14 y) of aging and modeling results that extends the prediction to 1×10^6 h (114 y) are presented. The prediction was benchmarked by the testing results of samples aged to 18,440 h (2.1y). To summarize, we have demonstrated the following key findings:

- Accelerated precipitation: The LPBF 316H SS exhibits precipitation kinetics that are 10–100 times faster than its wrought counterpart due to the presence of an extremely high density of preferred intragranular nucleation sites coupled with the elemental segregation on CBs and GBs. For the first time, the TTP diagram for a LPBF 316H SS was constructed and compared to that for the wrought, providing crucial information into the microstructural stability under prolonged thermal exposure in LPBF materials.
- Strength degradation: Thermal aging of LPBF 316H SS results in progressive dislocation recovery, precipitation coarsening, and solute depletion, leading to a notable decline in its tensile strength.
- Strength prediction: A multi-component physics-informed model was developed to model the evolution of $M_{23}C_6$ and Laves phases, which was used to predict the strength reduction factors up to 1×10^6 hours (114 years). The result show that while the LPBF 316H SS

undergoes more substantial strength loss, it retains higher strength compared to the conventional wrought 316H SS over long-term aging.

This study establishes a robust methodology for evaluating the long-term thermal stability of additively manufactured materials and highlights the importance of considering unique microstructural features when assessing their viability for high-temperature applications. These findings support the continued development and rapid qualification of LPBF 316H SS for nuclear and energy sector applications where long-term material reliability is essential.

4 Thermal aging of solution-annealed LPBF 316H

Section 3 studied the thermal aging effect on microstructure and tensile strength in an as-built LPBF 316H. In this section, we focus on the thermal aging of a solution-annealed (SA) LPBF 316H. The solution annealing condition was 1100°C, 1 h. Previous studies [35,36] show that under this SA condition, the materials do not recrystallize. The SA materials no longer have well-defined dislocation cells but instead, they have a high density of low-angle grain boundaries (LAGBs) of polygon shapes consisting of geometrically necessary dislocations (GNDs). The dislocation densities remain high, roughly at 1×10^{14} /m^2, which is about 5 times less than the AB materials. The dislocations have relaxed morphology and often have nano-oxides associated with them.

The thermal aging of SA LPBF 316H is initiated in FY25 and continuing. The aging is done at 550, 650, and 750°C, the same as the study on AB LPBF 316H (Section 3). At the time of writing this report, specimens aged to 2,500 h became available. Figure 18 shows the tensile curves of those specimens, which are in horizontal (denoted as "H") or vertical (denoted as "V") orientations. The test temperature was the same as the aging temperature. Also included in Figure 18 for comparison purposes are the tensile curves of unaged and 10,000-h WT 316H specimens. It is seen that the LPBF material behaves very differently from the WT material in terms of strength and ductility.

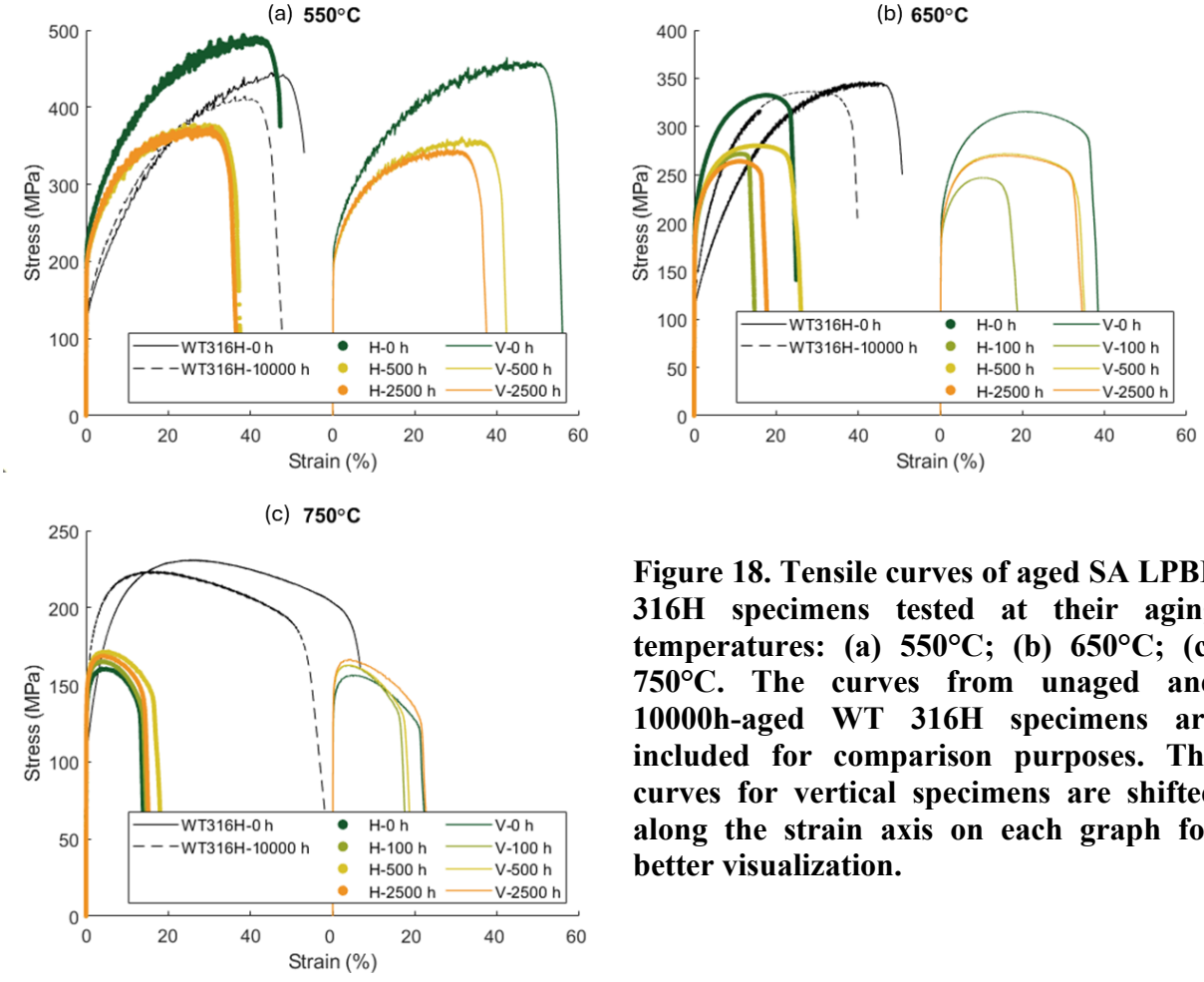

Figure 18. Tensile curves of aged SA LPBF 316H specimens tested at their aging temperatures: (a) 550°C; (b) 650°C; (c) 750°C. The curves from unaged and 10000h-aged WT 316H specimens are included for comparison purposes. The curves for vertical specimens are shifted along the strain axis on each graph for better visualization.

Figure 19 plots the tensile properties of the aged SA LPBF 316H obtained from the curves in Figure 18. For YS and UTS, the ASME Section III, Divion 5 specified design parameters for WT 316H are included as dashed lines. It is seen that while the LPBF 316H retains high YS upon aging, its UTS in general falls below the ASME design values for WT 316H. On the ductility side, the 750°C aged samples have poor UEL and TEL, with the UEL being only 4-5%.

Continued aging and testing as well as microstructural characterization will be performed in FY26.

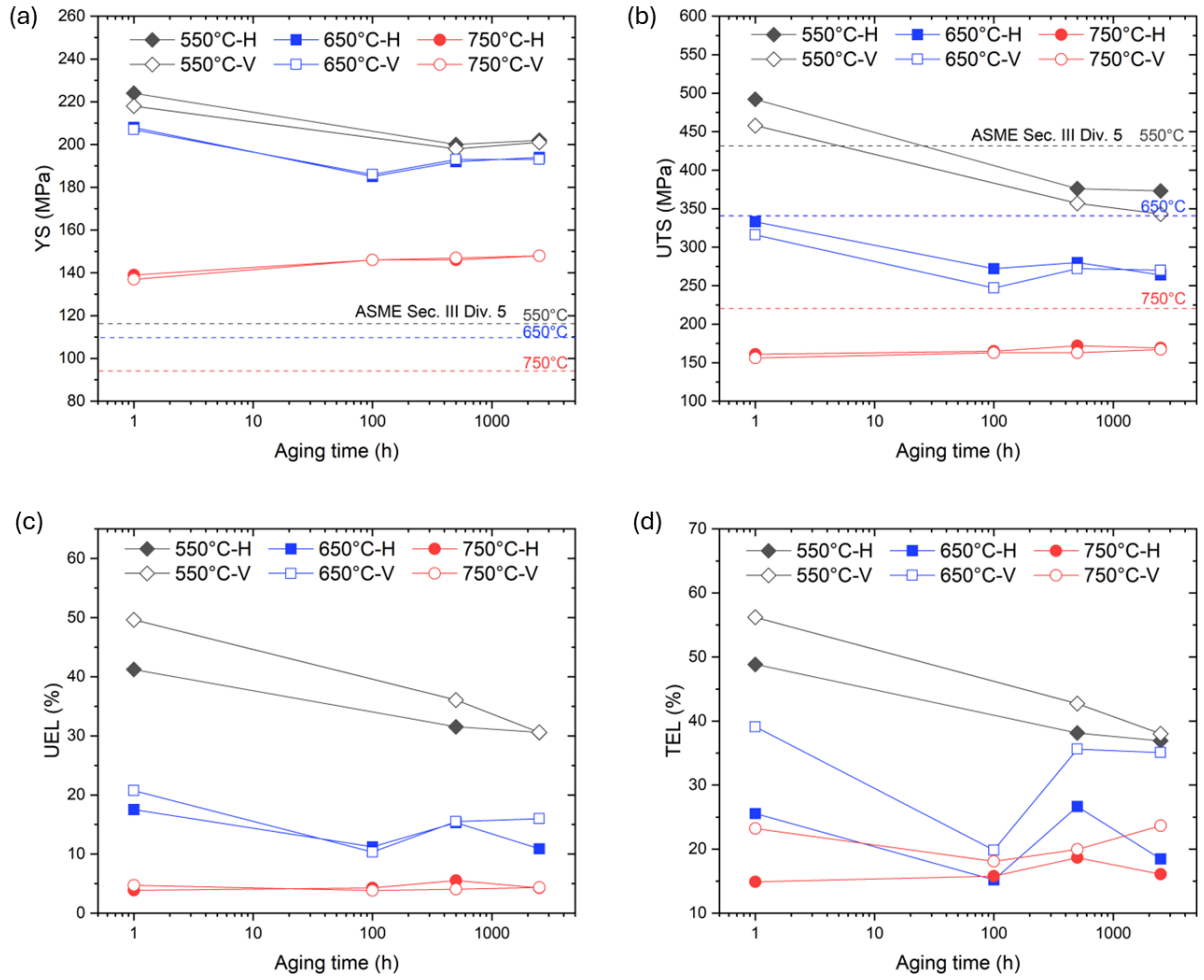

Figure 19. (a) Yield strength (YS) of aged SA LPBF 316H as a function of aging time. (b) Ultimate tensile strength (UTS) of aged SA LPBF 316H as a function of aging time. (c) Uniform elongation (UEL) of aged SA LPBF as a function of aging time. (d) Total elongation (TEL) of aged SA LPBF as a function of aging time. All tests were performed at the aging temperatures. For YS and UTS, the ASME Section III, Divion 5 specified design parameters for WT 316H are included as dashed lines.

5 Creep testing of LPBF 316H and WT 316H

5.1 Down-selection of solution-annealing as the heat treatment

Figure 20 (a) shows 62 creep-rupture tests completed at ANL and INL during FY24 and FY25, under three conditions listed in Table 5: 600°C/248 MPa, 725°C/100 MPa, and 800°C/53.3 MPa. These three conditions were chosen due to their predicted short creep-rupture times (hundreds of hours), so some understanding of the material's behavior can be obtained relatively quickly. The materials were printed on different machines, namely Renishaw AM400, GE Concept Laser M2, and EOS 290, used different batches of powders (see Table 1 and Table 2), and subsequently went through different heat treatments including stress relief (SR; 650°C for 24 h), solution annealing (SA; 1100°C for 1 h), and hot-isostatic pressing (HIP; 1150°C for 4 h at 100 MPa). It has been found that the creep behaviors of as-built (AB) and SR specimens are similar, so are SA and HIP specimens. Therefore, AB and SR specimens are grouped in Figure 20 (a), the same for SA and HIP specimens. Figure 20 (b) compares their creep rupture strains. It is seen that the LPBF specimens overall have lower creep rupture strains compared to the WT specimens. Under 725°C, 100 MPa, the AB/SR specimens have very low creep ductility (all below 10%), as highlighted by the dotted circle, while the SA/HIP specimens generally have creep rupture strains larger than 10%. For structural alloys, good creep ductility is desired to allow for stress redistribution in service and to prevent brittle, abrupt failures if creep cracking occurs. For this reason, the SA treatment is down-selected for the LPBF 316H material that is going into the first ASME code case. HIP treatment is not selected due to the much higher cost.

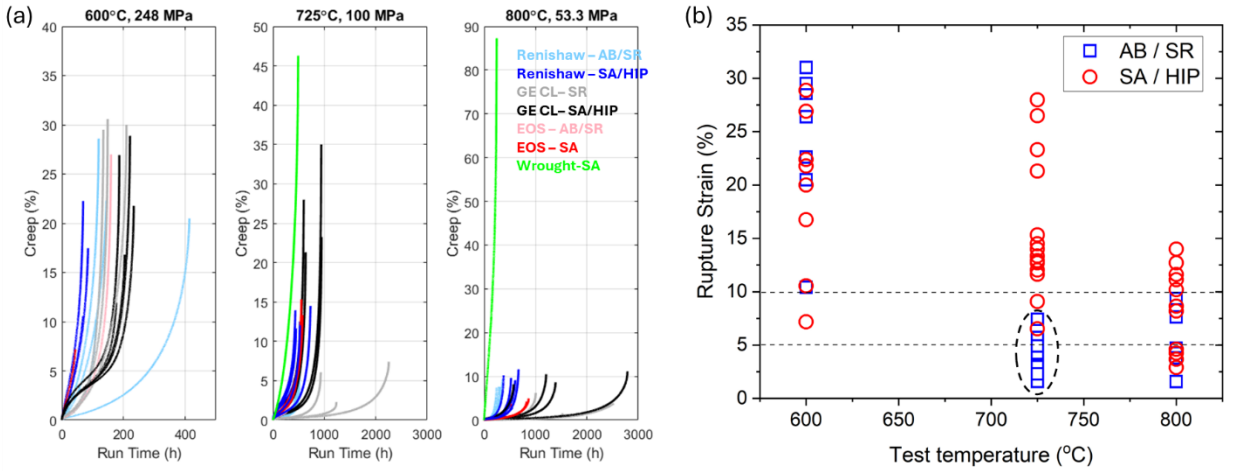

Figure 20. (a) Creep curves of various specimens tested under 600°C/248 MPa, 725°C/100 MPa, and 800°C/53.3 MPa. (b) Creep rupture strains of the specimens in (a).

Table 5. Short-term creep test conditions for SA LPBF 316H.

Temperature (°C)	Stress (MPa)
600	248
725	100
800	53.3

5.2 Creep behavior of SA LPBF 316H materials

Figure 21(a) includes the creep curves of a total of 29 tests on various batches of SA LPBF 316H materials and 2 tests on WT 316H under the three test conditions listed in Table 5. Figure 21(b) plots the 29 tests on SA LPBF 316H on top of the ASME database for WT 316H in the Larson-Miller plot. The Larson-Miller parameter (LMP) is calculated as:

$$LMP = (T + 273.15) \cdot (C + \log(t)),$$

where T is the temperature in °C, C is a constant taken as 16.28 [37], and t is the rupture time. Figure 21(b) shows that SA LPBF are largely within the scatter band of the WT, with the performance at the lower stress end seemingly better.

Figure 21(c) plots the minimum creep rate of the SA LPBF 316H specimens as a function of test temperature for the three creep conditions listed in Table 5. The two data points from WT 316H specimens are also included. Despite the large scatter, SA LPBF consistently has lower minimum creep rates compared to WT.

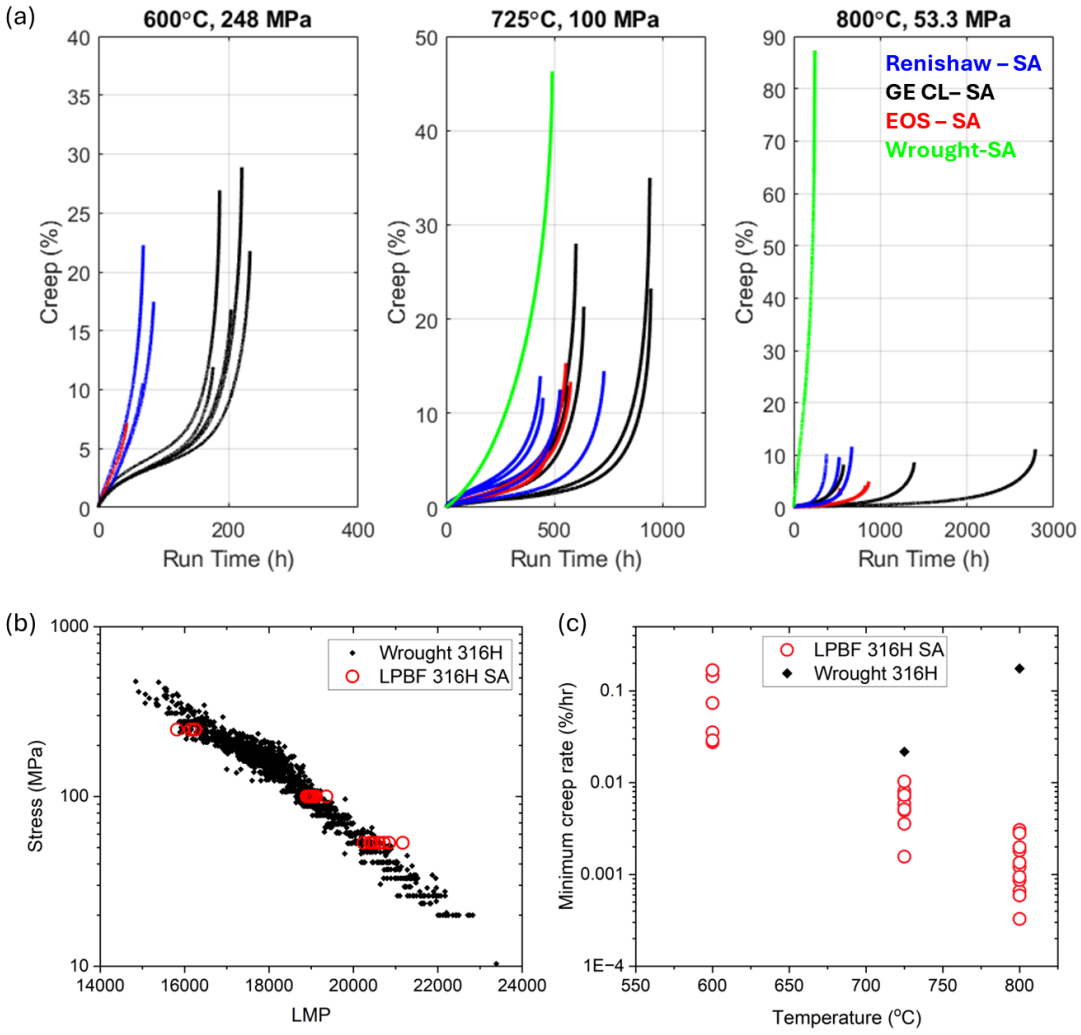

Figure 21. (a) Creep curves of various batches of SA LPBF 316H tested under conditions listed in Table 5. (b) Larson-Miller plot of SA LPBF 316H data points on top of the ASME data for WT 316H. (c) Minimum creep rates of SA LPBF 316H as a function of test temperature under conditions listed in Table 5; two data points on WT 316H are included.

In FY25, another set of creep conditions have been determined with anticipated rupture times of thousands of hours. Table 6 lists the temperatures and stress levels. At the time of writing this report, 14 tests on various batches of LPBF 316H materials are running, with more in queue. Those results will be reported in FY26.

Table 6. Mid-term creep test conditions for SA LPBF 316H.

Temperature (°C)	Stress (MPa)
600	180
650	124
725	71
800	36

5.3 Understanding the creep ductility issue

Figure 20 (b) shows a creep ductility dip of SA LPBF 316H at 800°C. To understand this phenomenon, a number of ruptured specimens under each test condition were sectioned at the middle of the fracture tip area along the loading direction. Table 7 lists the specimens investigated, covering materials printed with two Renishaw AM400 machines and a GE Concept Laser M2 machine. Figure 22 and Figure 23 show the SEM-BSE images of the exposed areas in those samples near the fracture tip. In the images with lower magnification (Figure 22), no prominent features stand out in the 600 and 725°C tested samples. In contrast, the 800°C tested samples have bright precipitates decorating the pre-existing grain boundaries. Those precipitates are rich in Mo and are likely the sigma phase as observed in aged samples as described in Section 3 and Section 4. In the images with higher magnifications (Figure 23), it is seen that those sigma phase precipitates at 800°C are promoting the formation and propagation of long cracks, which is expected to lead to premature failures and low creep rupture strains.

Table 7. List of SA LPBF 316H specimens investigated for creep ductility issue.

Build ID	Machine	Heat treatment	T (degC)	Stress (MPa)	Time to rupture (hr)	Creep strain machine (%)
ANL-B1	Renishaw AM400	SA	600	248	69	22.3
ORNL-ANL-best	Renishaw AM400	SA	600	248	69	10.55
ORNL-B2	Concept Laser	SA	600	248	204	16.80
Wrought		SA	725	100	490.5	46.26
ORNL-ANL-best	Renishaw AM400	SA	725	100	447	11.64
ORNL-B2	Concept Laser	SA	725	100	636	21.31
ORNL-B1	Concept Laser	SA	725	100	945	23.24
ANL-B1	Renishaw AM400	SA	800	53.3	525	9.63
ORNL-ANL-best	Renishaw AM400	SA	800	53.3	553	2.90

ORNL-B1	Concept Laser	SA	800	53.3	2789	11.13

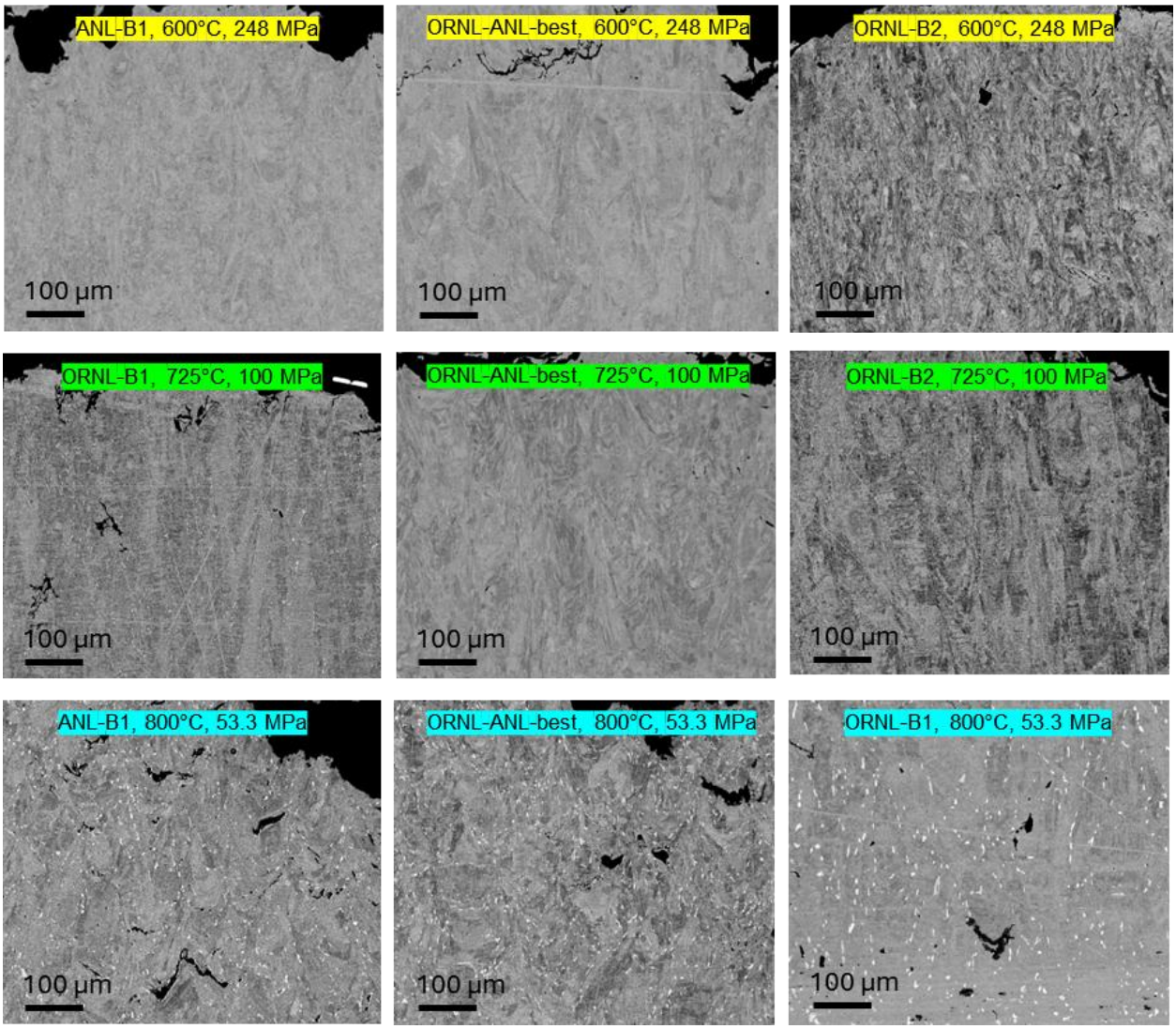

Figure 22. SEM-BSE images of LPBF 316H specimens creep-ruptured under different conditions (200×).

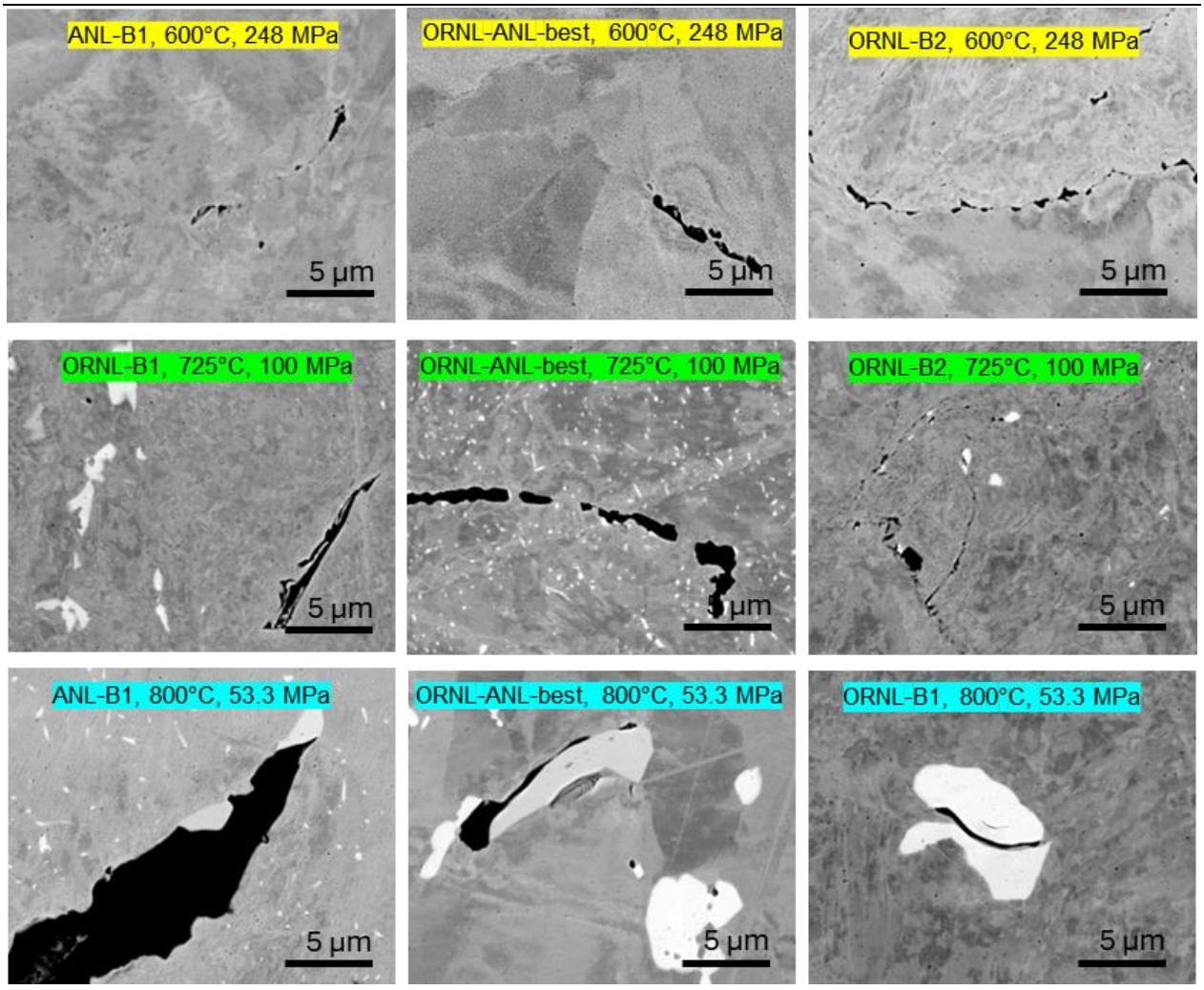

Figure 23. SEM-BSE images of LPBF 316H specimens creep-ruptured under different conditions (5000×).

The precipitation of sigma phase is not unique to LPBF 316H. As shown in Section 3 and in Figure 10, sigma phase forms in WT 316H upon extended aging. The effect of the sigma phase precipitates on the creep ductility of WT 316H has been recognized, which attributes some accelerated failures to more pronounced formation of these embrittling phases (see Ref. [38] and references cited therein). In this research, we performed creep tests on WT 316H under two conditions that are also used in testing LPBF 316H materials: 800°C, 53.3 MPa and 800°C, 36 MPa. The goal is to provide direct evidence on the role of sigma phase particles on creep cracking.

Figure 24(a) shows the creep curves of the two tests. Notably, the longer test has a much lower creep rupture strain. Figure 24(b) shows the cross-sectional optical images of areas near the fracture tips of the two specimens. It is evident that the specimen tested under 800°C, 36 MPa (with lower rupture strain) has extensive wedge cracking while the other has limited cavitation.

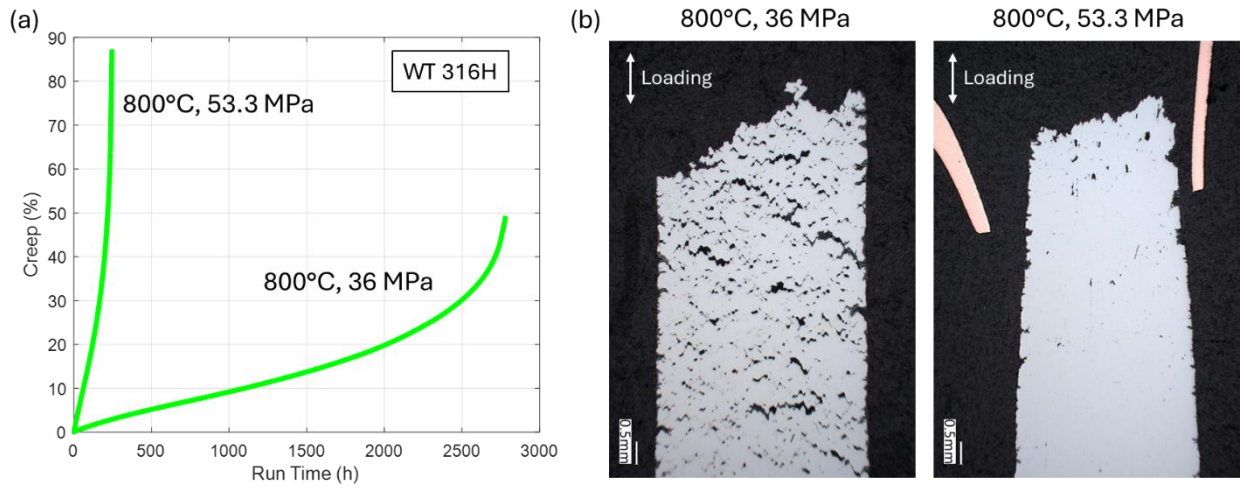

Figure 24. (a) Creep rupture curves of WT 316H specimens tested at 800°C, 36 MPa and 800°C, 53.3 MPa. (b) Cross-sectional optical images of areas near the fracture tips of the two specimens.

Figure 25 shows the SEM-BSE images of the areas near the fracture surfaces of the two specimens. The wedge cracking in the specimen tested under 800°C, 36 MPa (Figure 25(a)) is evidently related to the bright precipitates that decorate the grain boundaries. The two higher magnification images in Figure 26 further prove that those large precipitates are brittle and play a vital role in advancing cracks. In contrast, Figure 25(b) shows that without those brittle particles, the creep cavitation in the specimen tested under 800°C, 53.3 MPa are blunted and less prone to cracking.

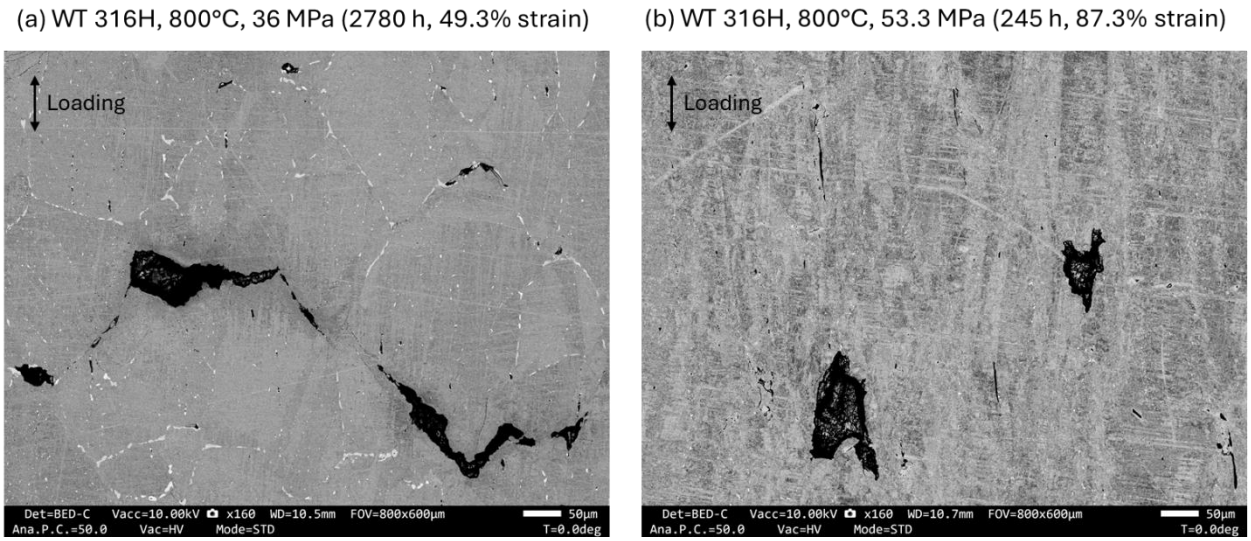

Figure 25. (a) An SEM-BSE image of an area near the fracture surface in a WT 316H specimen tested at 800°C, 36 MPa. (b) An SEM-BSE image of an area near the fracture surface in a WT 316H specimen tested at 800°C, 53.3 MPa.

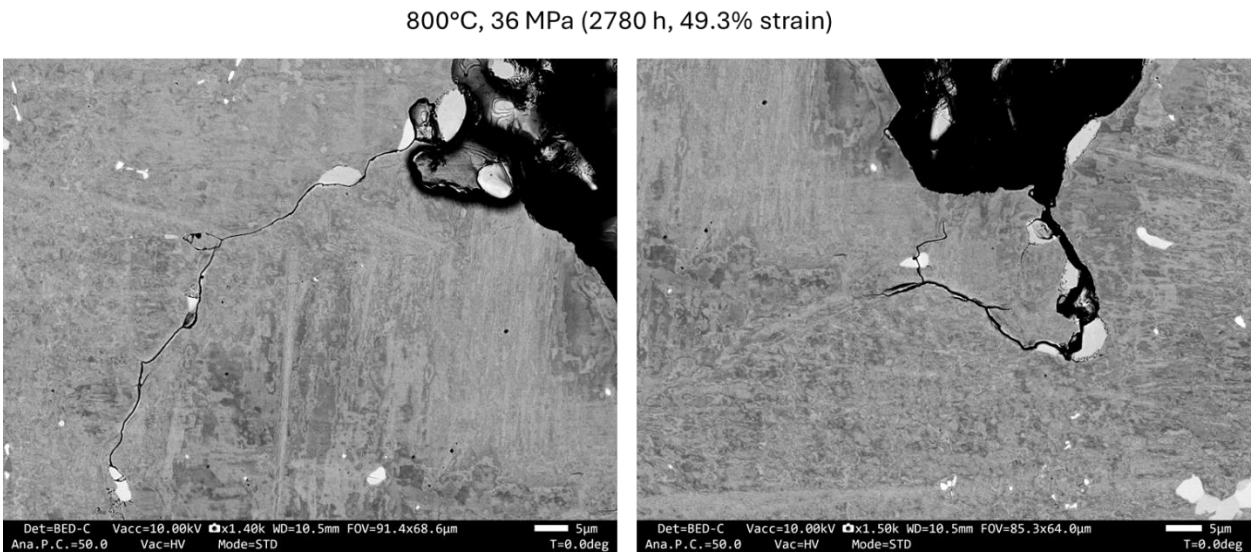

Figure 26. SEM-BSE images of a WT 316H specimen tested at 800°C, 36 MPa, showing crack propagation along chains of sigma phase precipitates.

The bright precipitates in the specimen tested under 800°C, 36 MPa are enriched in Cr and Mo, as shown in Figure 27. Per discussions in Section 3.2.2, those precipitates are likely the sigma phase, although x-ray diffraction or electron diffraction is needed to confirm their crystallographic structure. Sigma phase is not observed in the specimen tested under 800°C, 53.3 MPa; instead, the small, bright precipitates observed in SEM-BSE images are Mo-Si rich (Figure 28), which are likely the Laves phase per discussions in Section 3.2.2. Given that the two specimens were tested at the same temperature, the only reason that the sigma phase was formed in the 800°C, 36 MPa specimen is its much longer test duration (2780 h) compared to the other (245 h). Assuming that the precipitation kinetics in a heavily creep-deformed material is similar to that in an LPBF material, the TTP diagram in Figure 10 shows that the sigma phase forms upon hundreds of hours of aging at 800°C, in rough agreement with the observations here.

One common observation in both specimens is the Cr-rich carbide precipitates (see Figure 28 as an example). The carbides form on dislocations, twin boundaries, and grain boundaries. They also form next to the Laves or sigma phase particles. They pin dislocations and have a dominant role in steady-state creep, and may have a synergistic role along with the sigma phase in pre-mature creep rupture, although it is less evident that they are as brittle as the sigma phase (i.e., no cracking across carbides has been observed).

The observations in this section on creep-ruptured LPBF 316H and WT 316H materials suggest that the extended sigma phase formation along grain boundaries is a key mechanism in creep rupture and is responsible for the reduced creep ductility. The accelerated precipitation in LPBF materials as discussed in Section 3, coupled with their much smaller grain sizes (i.e. larger grain boundary areas, see Figure 29) compared to the WT, leads to the early formation of a high density of embrittling sigma phases, resulting in their very low creep ductility.

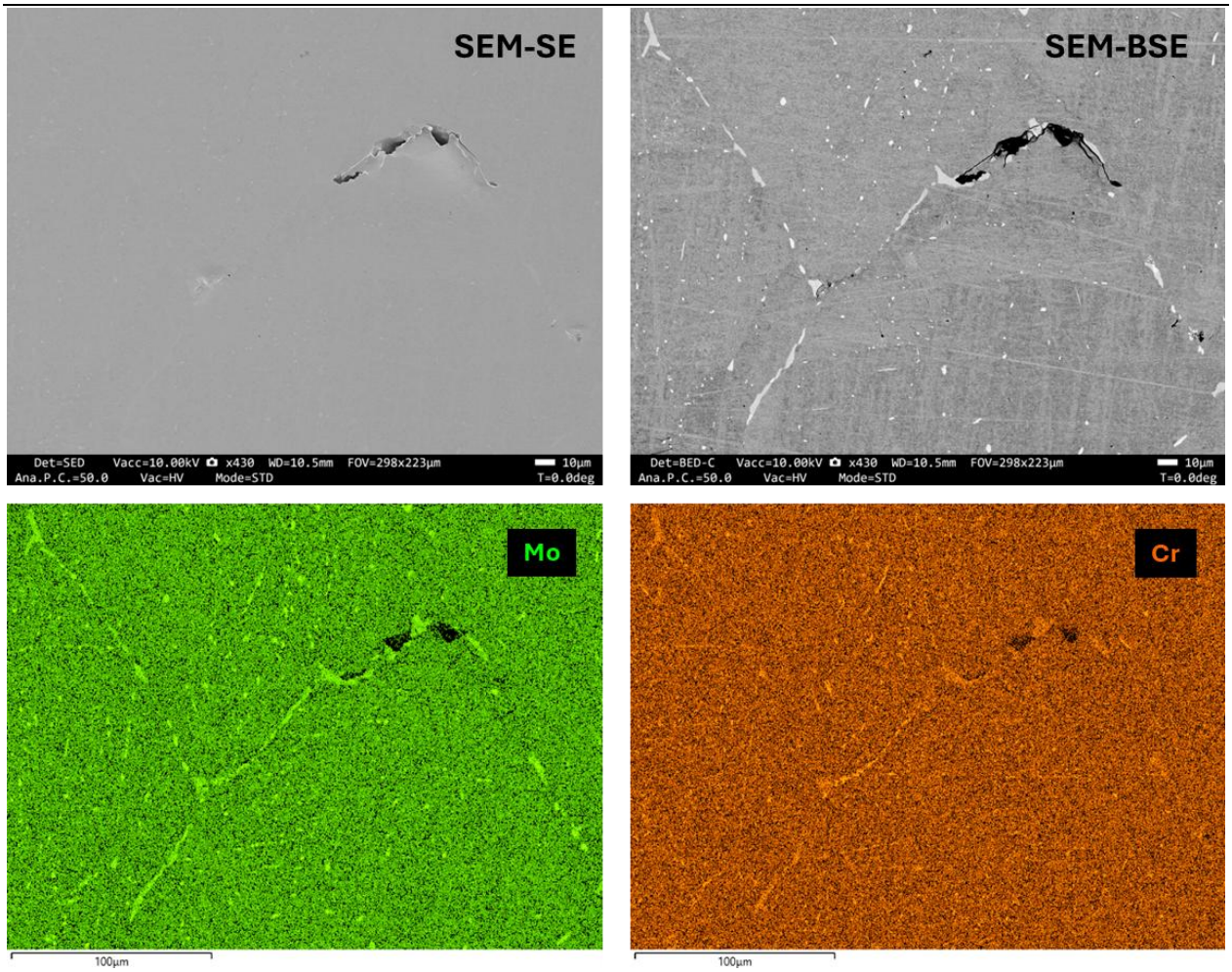

Figure 27. SEM-SE and SEM-BSE images of an area near the fracture surface in a WT 316H specimen tested at 800°C, 36 MPa, along with the EDS maps of Cr and Mo.

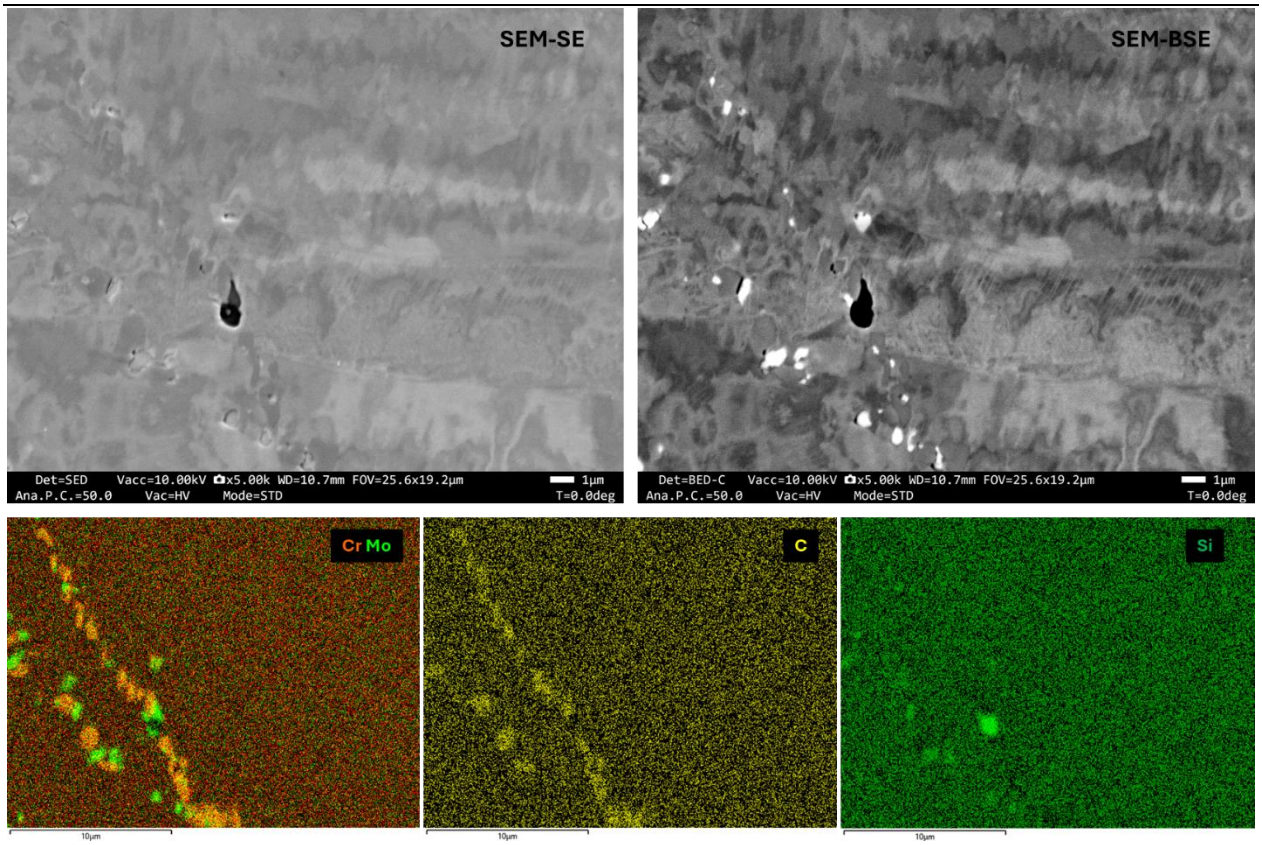

Figure 28. SEM-SE and SEM-BSE images of an area near the fracture surface in a WT 316H specimen tested at 800°C, 53.3 MPa, along with the EDS maps of Cr, Mo, C, and Si.

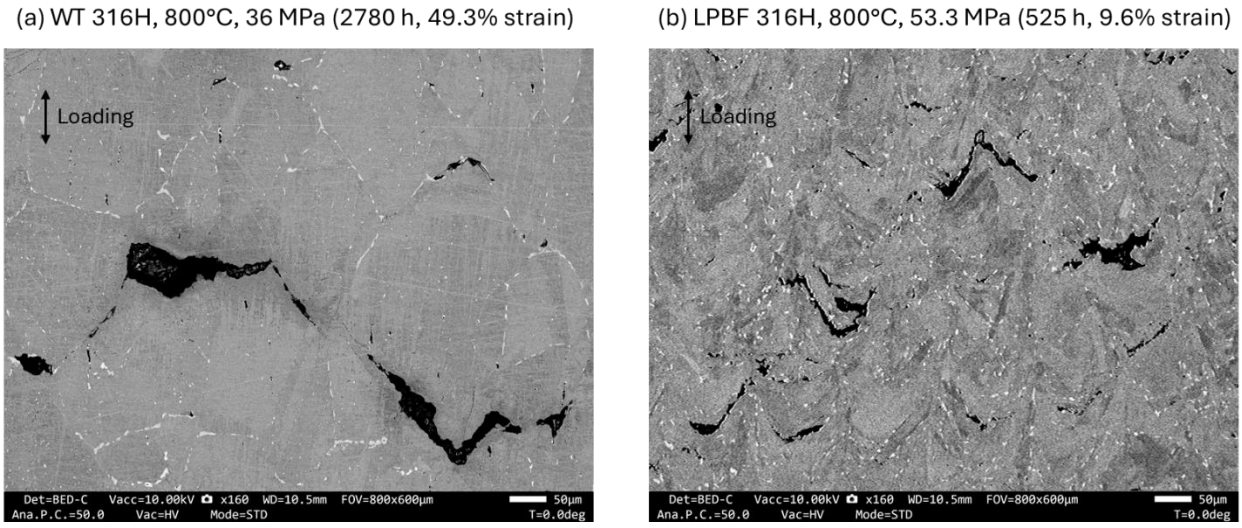

Figure 29. (a) An SEM-BSE image of an area near the fracture surface in a WT 316H specimen tested at 800°C, 36 MPa. (b) An SEM-BSE image of an area near the fracture surface in an LPBF 316H specimen tested at 800°C, 53.3 MPa. The bright particles in those images are sigma phases.

6 Fatigue and creep-fatigue testing of LPBF 316H

6.1 Test results

A total of 40 fatigue and creep-fatigue tests have been performed so far on five LPBF builds. Samples with and without post-build heat treatments were included. The testing effort in FY25 was focused on the samples with SA treatment. Specimens printed with different LPBF systems and extracted from different orientations with respect to the build direction were tested. In addition, several creep-fatigue tests with long hold time (60 min) were conducted with SA samples at 595°C to assess the acceptability of the current materials. All cyclic tests were conducted in a fully reversed, strain-controlled mode, and were performed with a nominal strain amplitude of 0.5% and a strain rate of 0.1%/s. The test results to date are summarized in Table 8. Note that the cyclic lives were defined differently between the two laboratories: ANL used a 25% load drop, while INL used a 20% load drop. Nonetheless, the differences in cyclic life between these two definitions were negligibly small due to the rapid load change at the end of the cyclic test.

Table 8. Fatigue and creep-fatigue test results on AM 316H SS

AM build	Sample ID	Heat treatment [1]	Test temperature (°C)	Strain AMP (%)	Hold time (min)	Cyclic life [2] (cycles)
ANL-B1	51-1-F3	AB	550	0.5	-	775
	51-2-F3	SA	550	0.5	-	356
	51-3-F3	SR	550	0.5	-	896
	51-4-F3	HIP	550	0.5	-	1062
	51-1-F2	AB	550	0.5	6	403
	51-2-F2	SA	550	0.5	6	330
	51-3-F2	SR	550	0.5	6	742
	51-4-F2	HIP	550	0.5	6	720
ANL-B2	35-3-F1	SA	595	0.5	60	144
	35-3-F2	SA	550	0.5	6	394
	35-4-F1	SA	550	0.5	6	179
	35-4-F2	SA	550	0.5	-	985 [3]
	35-4-F3	SA	595	0.5	60	72 [3]
ORNL-B1	B1P7B-2	SR	550	0.5	6	2350
	B1P7B-3	SR	550	0.5	-	2155
	B1P8B-1	SA	550	0.5	6	2225
	B1P8B-2	SA	550	0.5	-	2710
	B1P9B-1	HIP	550	0.5	6	1481
	B1P9B-2	HIP	550	0.5	-	2255
	B4P8-4	SA	550	0.5	-	1186
	B1P7-H-F1	SA	550	0.5	6	454 [3]
	B1P7-H-F2	SA	550	0.5	-	931
	B1P7-H-F3	SA	595	0.5	60	70 [3]
ORNL-ANL-best	H1-ANL-Best-02-10	SR	550	0.5	-	1315
	H1-ANL-Best-02-11	SR	550	0.5	6	817
	H2-ANL-Best-02-23	SA	550	0.5	-	333 [3]
	H2-ANL-Best-02-24	SA	550	0.5	6	243

LANL-INL-2	LCF-1	SR	550	0.5	30	567
	LCF-2	SR	550	0.5	6	2037
	LCF-3	SR	650	0.5	30	302
	LCF-4	SR	650	0.5	-	1313
	LCF-6	SA	550	0.5	6	1037
	LCF-7	SA	550	0.5	-	2191
	LCF-8	SA	650	0.5	30	168
	LCF-9	SA	650	0.5	-	1070 [3]
	LCF-11	SA	750	0.5	-	994
	LCF-12	SA	750	0.5	30	317
	LCF-13	SA	750	0.5	6	291
	LCF-14	SA	650	0.5	6	229
	LCF-15	SA	595	0.5	60	165

[1] As Built = AB, Solution Annealed = SA, Stress Relieved =SR, and Hot Isostatic Pressed = HIP
[2] For the tests conducted on ANL-B1 and ORNL-B1, failure lives were recorded at 25% load drop. For the tests on the AM build LANL-INL-2, failure lives were recorded at 20% load drop.
[3] Cracking occurred outside of the extensometer gauge.

6.2 Compare AM builds produced from different LPBF systems

Test results from FY24 showed that LPBF materials produced at different laboratories exhibited consistently different cyclic responses in both fatigue and creep–fatigue tests [3]. One laboratory used a Renishaw AM 400 equipped with a pulsed-wave (PW) laser, while the other used a GE Concept Laser system with a continuous-wave (CW) laser. It is not clear whether the observed differences stem from the respective process parameter sets or from the laser temporal mode (PW vs. CW) of the LPBF systems. To enable a more controlled comparison, an additional batch of AM 316H stainless steel was produced this fiscal year on a different Renishaw platform by a different laboratory. The test results are summarized in Table 9 and are compared with previous tests conducted on samples produced from different LPBF systems.

Table 9. Fatigue and creep-fatigue tests [1] on samples produced with different LPBF systems

Laser temporal mode [2]	Sample ID	Heat treatment	Hold time (min)	Cyclic life (cycles)
PW 1	51-3-F3	SR	-	896
PW 2	H1-ANL-Best-02-10	SR	-	1315
CW	B1P7B-3	SR	-	2155
PW 1	51-2-F3	SA	-	356
PW 2	H1-ANL-Best-02-23	SA	-	333 [3]
CW	B1P8B-2	SA	-	2710
PW 1	51-3-F2	SR	6	742
PW 2	H1-ANL-Best-02-11	SR	6	817
CW	B1P7B-2	SR	6	2350
PW 1	51-2-F2	SA	6	330
PW 2	H1-ANL-Best-02-24	SA	6	243
CW	B1P8B-1	SA	6	2225

[1] All cyclic tests were performed with 0.1%/s strain rate, 0.5% strain amplitude, and a load ratio of -1.
[2] PW = Pulsed wave, CW = continuous wave
3 Cracking occurred outside of the extensometer gauge.

Figure 30 shows the stress amplitude profiles from cyclic tests on stress-relieved (SR) and solution-annealed (SA) samples. While SR specimens exhibited brief cyclic hardening followed by extended softening, SA specimens showed sustained cyclic hardening throughout testing. For both SR and SA conditions, samples produced with two pulsed laser systems from two different laboratories showed similar behavior. Samples printed with the CW laser platform (the green curves in Figure 30) consistently outperformed those printed with the PW laser systems.

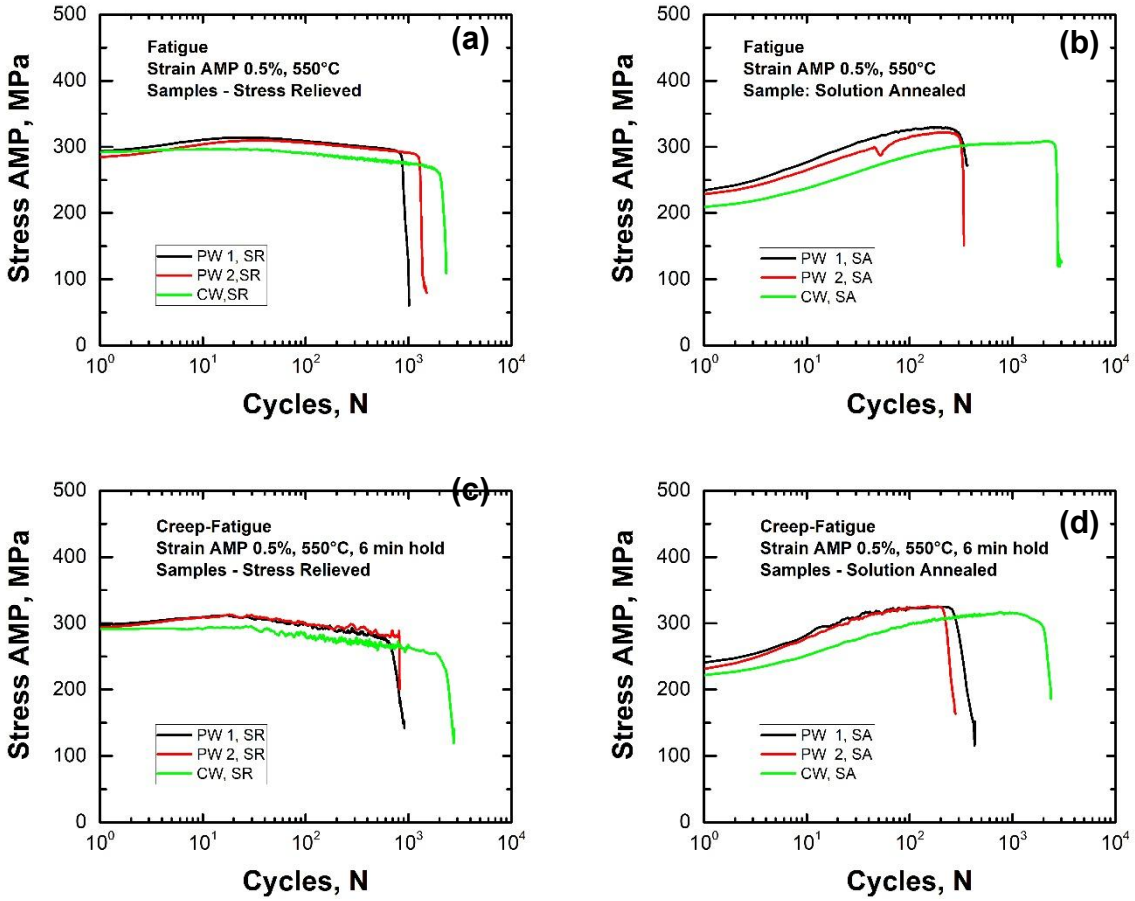

Figure 30. Stress amplitude profiles of fatigue and creep-fatigue tests performed on materials produced with different LPBF systems. (a) fatigue tests on SR samples, (b) fatigue tests on SA samples, (c) creep-fatigue tests on SR samples, and (d) creep-fatigue tests on SA samples.

Figure 31 shows the hysteresis loops at the half-life of the samples printed with different LPBF systems. At the steady state, the hysteresis loops of the samples produced with CW laser (i.e., the blue hysteresis loops in Figure 31) are slightly lower than those printed with PW laser. It appears that use of a CW laser contributes to the favorable cyclic performance. The positive impact of CW on the cyclic performance of LPBF materials is more evident for the SA samples than for the SR samples. Additional testing and microstructural characterization are needed to isolate this laser mode effect from process parameter and microstructural influences.

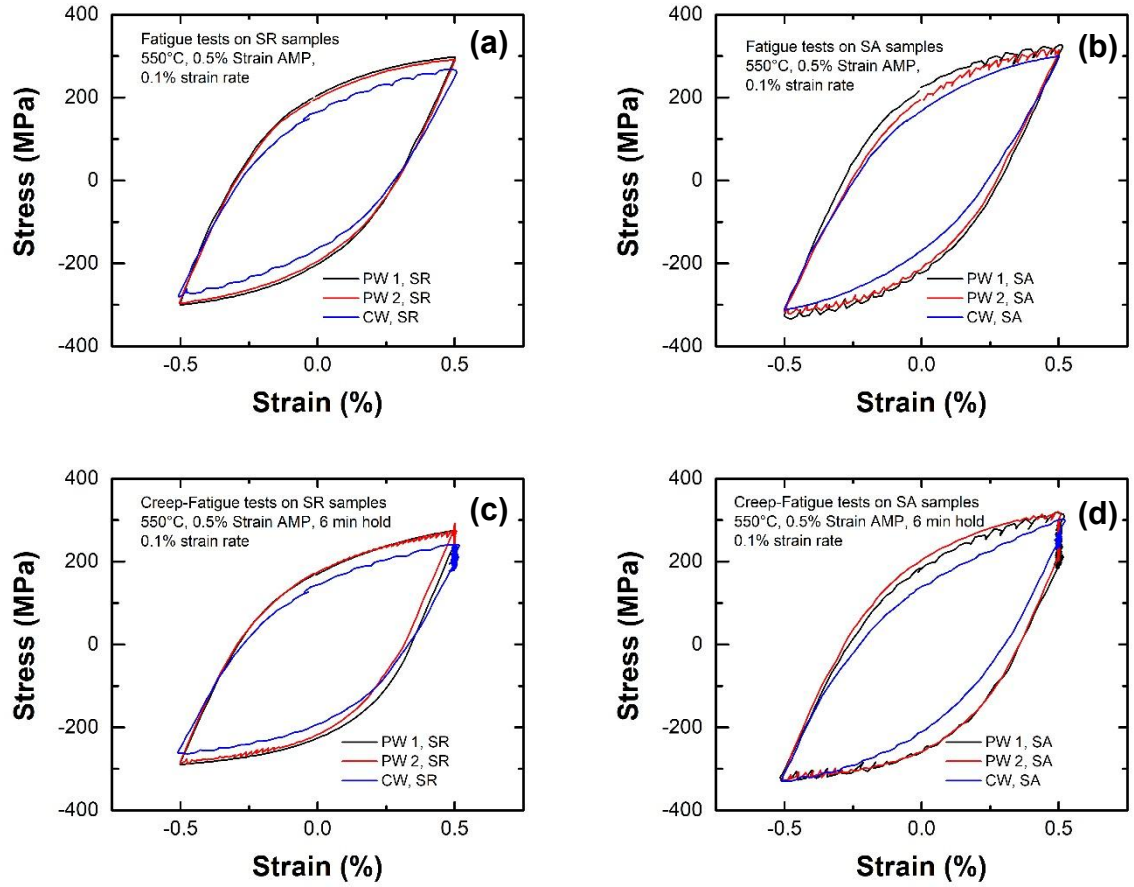

Figure 31. Hysteresis loops at the half-life for materials produced from different LPBF system; (a) fatigue tests on SR samples, (b) fatigue tests on SA samples, (c) creep-fatigue tests on SR samples, and (d) creep-fatigue tests on SA samples.

6.3 Compare LPBF samples with different orientations

LPBF materials often exhibit anisotropy due to their layer-by-layer deposition. Unlike conventional manufacturing, the building process of LPBF materials can introduce microstructural and property variations across different orientations. To investigate the effect of orientation on cyclic response, we extracted samples from both build direction and transverse direction and tested them under identical conditions. Table 10 shows the test results. All tests were conducted on SA samples with a strain amplitude of 0.5% and a strain rate of 0.1%/s. Since PW and CW laser modes may influence cyclic performance, comparisons were made with the same laser mode.

Table 10. Fatigue and creep-fatigue tests[1] on samples with different build direction

Laser temporal mode	Sample orientation	Sample ID	Heat treatment	Hold time (min)	Cyclic life (cycles)
PW	Transverse	35-4-F2	SA	-	985 [2]
	Build	51-2-F3	SA	-	356
	Build	H2-ANL-Best-02-23	SA	-	333 [2]
	Transverse	35-4-F1	SA	6	179
	Build	35-3-F2	SA	6	394

	Build	51-2-F2	SA	6	330
	Build	H2-ANL-Best-02-24	SA	6	243
CW	Transverse	B1P7-H-F2	SA	-	931
	Build	B4P8-4	SA	-	1186
	Build	B1P8B-2	SA	-	2710
	Transverse	B1P7-H-F1	SA	6	454 [2]
	Build	B1P8B-1	SA	6	2225

[1] All cyclic tests were performed with 0.1%/s strain rate, 0.5% strain amplitude, and a load ratio of -1.
[2] Cracking occurred outside of the extensometer gauge.

Figure 32 shows the evolution of stress amplitude during cyclic testing. In each plot, the black curve corresponds to the transverse-direction sample, and the colored curves correspond to the build-direction samples. Overall, transverse-direction samples show greater cyclic hardening than build-direction samples. With only one exception (Figure 32(a)), the cyclic lives of transverse-direction samples are shorter than those of build-direction samples. For the PW-laser builds (Figure 32 (a) and (b)), the effect of sample orientation is inconclusive. It is not clear if the longer fatigue life observed in the transverse-direction sample reflects a true trend or an outlier. Additional testing is needed to clarify the impact of sample orientation on the fatigue life of LPBF 316H SS.

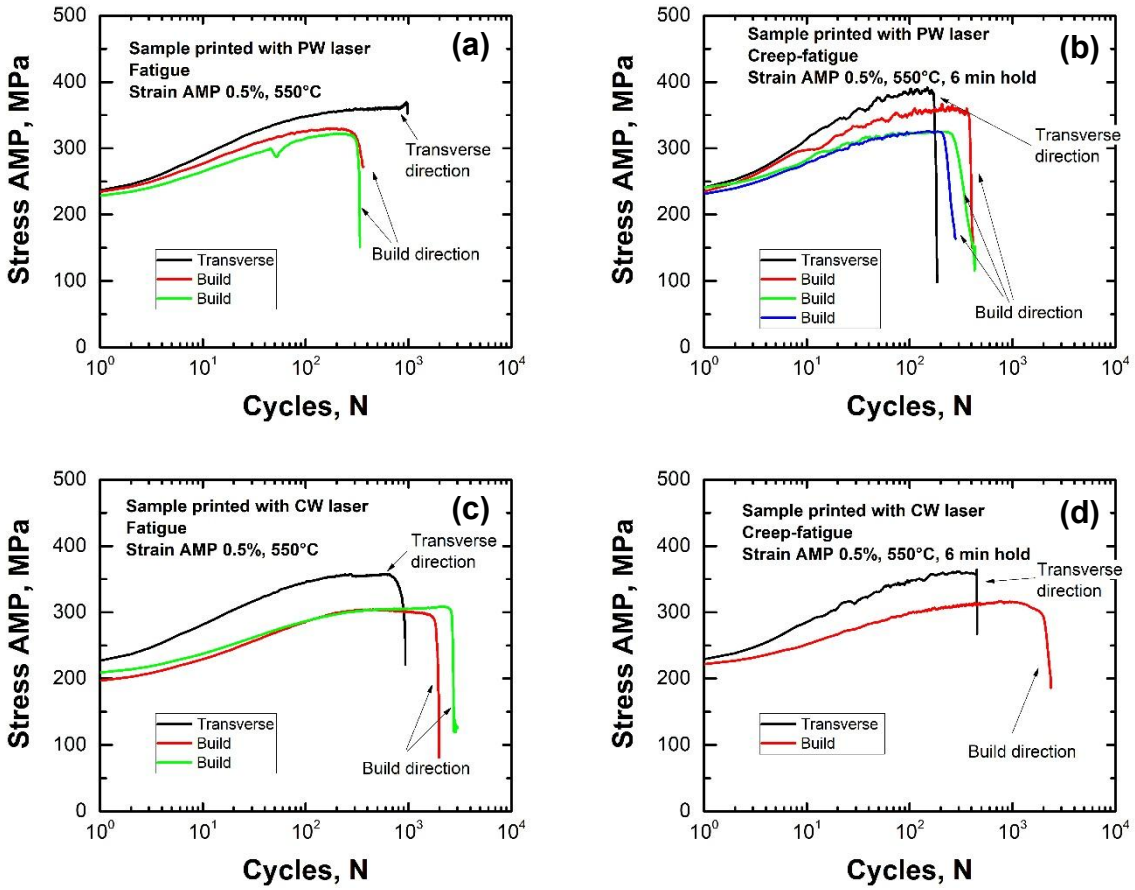

Figure 32. Comparison of fatigue and creep-fatigue tests performed on samples extracted from the transverse and build directions. (a) Fatigue tests on sample produced with PW

laser, (b) creep-fatigue tests on sample produced with PW laser, (c) fatigue tests on sample produced with CW laser, (b) creep-fatigue tests on sample produced with CW laser

6.4 Long-hold-time acceptance tests

Based on BPVC Section III Division 5, the creep-fatigue life of a WT 316H material should exceed 200 cycles when tested at 595℃ with a strain amplitude of 0.5% and 60 min hold time. To assess the performance of LPBF 316H SS under this requirement, several "acceptance" tests were performed on samples produced with different LPBF systems and in different orientations. All samples received a solution-anneal treatment (1 hour at 1100°C followed by water quench), and were tested with a strain rate of 0.1%/s. Table 11 summarizes the test results.

Table 11. Creep-fatigue tests[1] with 60-minute hold time at strain maximum

Laser temporal mode	Sample orientation	Sample ID	Heat treatment	Hold time (min)	Cyclic life (cycles)
CW	Transverse	B1P7-H-F3	SA	60	70 [2]
PW	Transverse	35-4-F3	SA	60	72 [2]
PW	Build	35-3-F1	SA	60	144
CW	Build	LCF-15	SA	60	165 [2]

[1] All cyclic tests were performed with 0.1%/s strain rate, 0.5% strain amplitude, and a load ratio of -1.

[2] Cracking occurred outside of the extensometer gauge.

As shown in Figure 33, all samples exhibited cyclic hardening as expected for SA samples. One sample produced with CW laser and tested in build direction showed somewhat lower cyclic strength than the other three, yielding the longest cyclic life among these samples. While no obvious laser-mode effect can be seen, the two samples in build direction outperform the samples in transverse direction considerably. It is evident that the orientation effect dominates the creep-fatigue response under this test condition.

A similar trend is observed in the hysteresis loops at the maximum stress amplitude. As shown in Figure 34, the CW-laser sample tested along the build direction exhibits a slightly smaller hysteresis loop compared with other samples. Although none of the samples passes the requirement outlined in BPVC Section III Division 5, optimized heat-treatment conditions may enable the build-direction sample to meet the criterion.

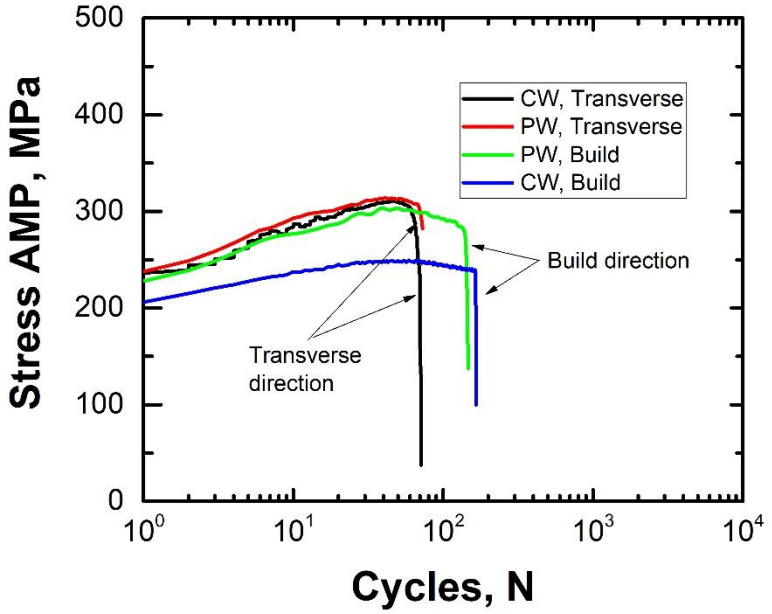

Figure 33. Creep-fatigue tests with 60-min hold time at strain maximum

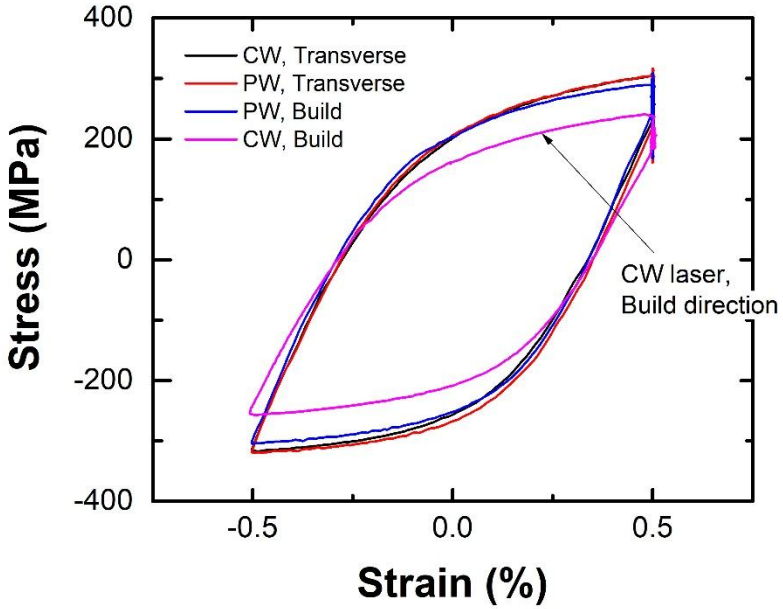

Figure 34. Hysteresis loops at the maximum stress amplitudes of 60-min hold time creep-fatigue tests

6.5 Cyclic performance at 650°C and 750°C

Fatigue and creep-fatigue tests performed at 750°C were completed in FY-25. Peak and valley stresses from fatigue (LCF-11) and creep-fatigue (LCF-12 and LCF-13) tests are compared in Figure 35. All cyclic tests were performed with 1% strain range, and hold times for CF tests are documented as 6 min or 30 min. Hysteresis loops at 10th cycle from these tests are compared in

Figure 36(a). At 750°C, cyclic relaxation is observed which was consistent with previous observations at 550°C and 650°C [3]. The hysteresis loops from creep-fatigue tests showed comparable behavior as that of fatigue. Comparison of stress against time plots are shown in Figure 36(b), where stress relaxation from creep-fatigue tests from 6 minutes and 30 minutes are presented.

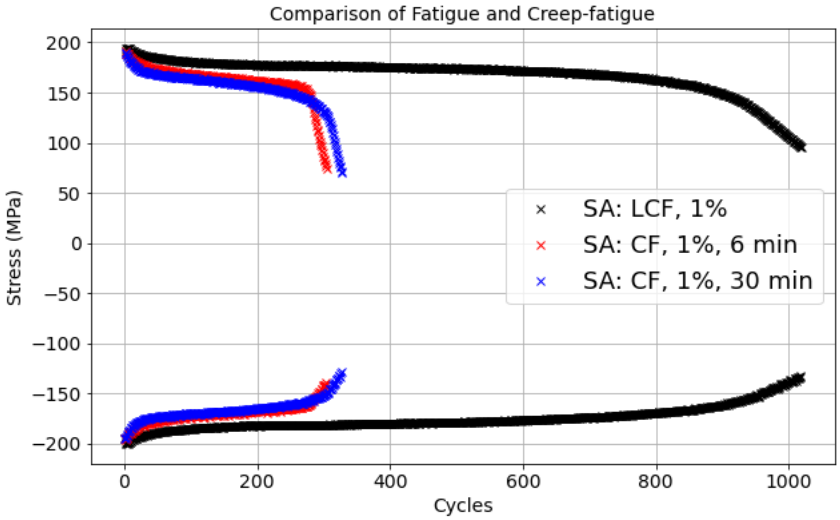

Figure 35. Comparison of the peak and valley stress plots from fatigue and creep-fatigue tests with 1% strain range at 750°C.

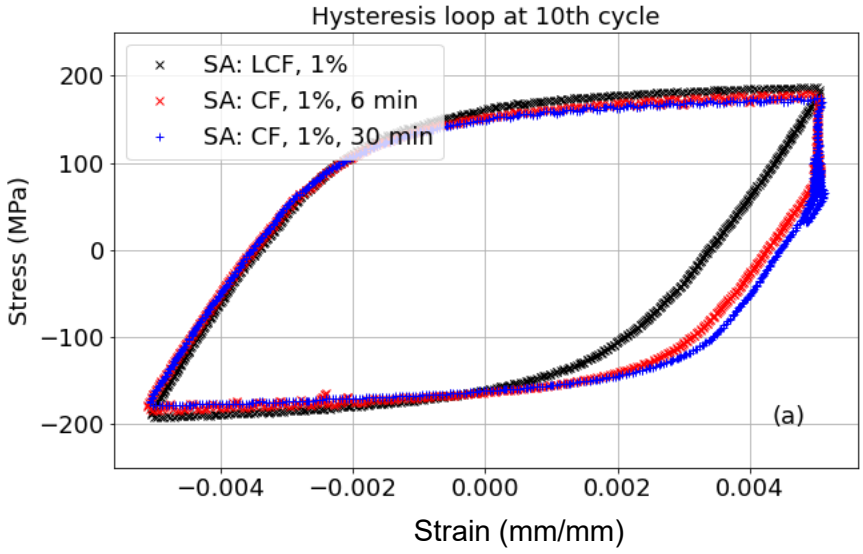

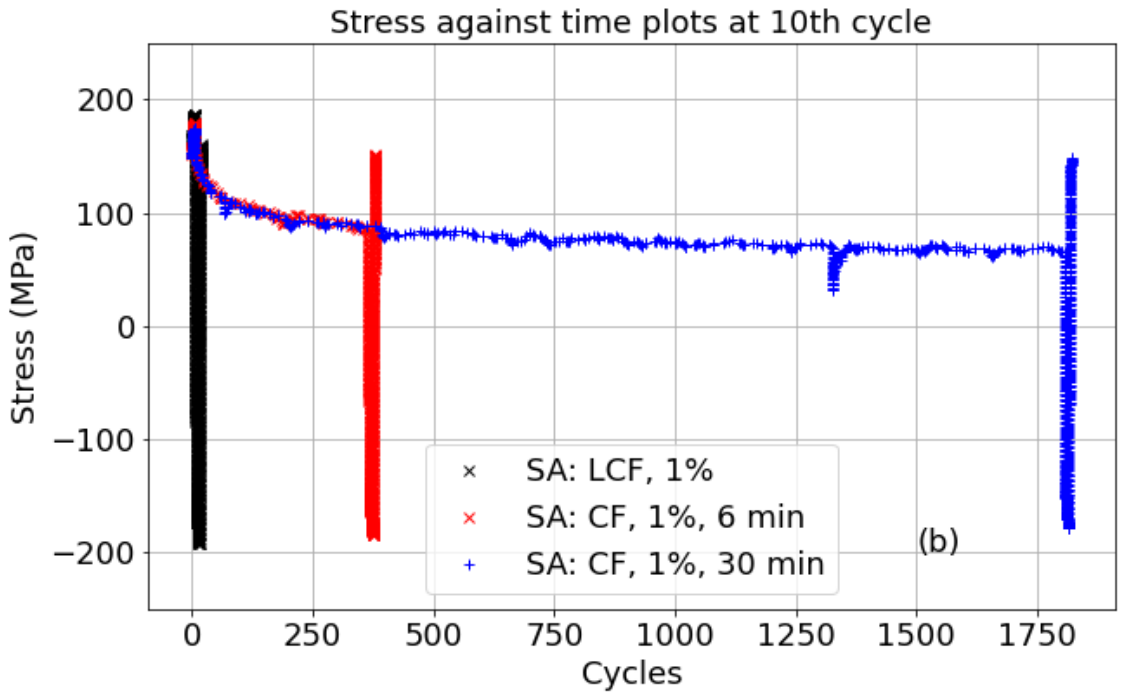

Figure 36. Comparison of (a) hysteresis loop, and (b) stress relaxation profile against time from fatigue and creep-fatigue tests with 1% strain range at 750°C.

Sample data from different heat treatments were compared. All cyclic specimens from LANL-INL-2 build were used in this comparison, and each set of specimens had SR or SA heat treatment. Stresses at peak and valley strains from fatigue and creep-fatigue samples with different heat treatments are compared in Figure 37. Note that fatigue specimen with SA state failed outside extensometer, which led to increased externally applied displacement which inevitably leads to increase in the peak and valley stress intensities near failure. The 10^{th} hysteresis loop and mid-life hysteresis loops from these tests are compared for reference in Figure 38.

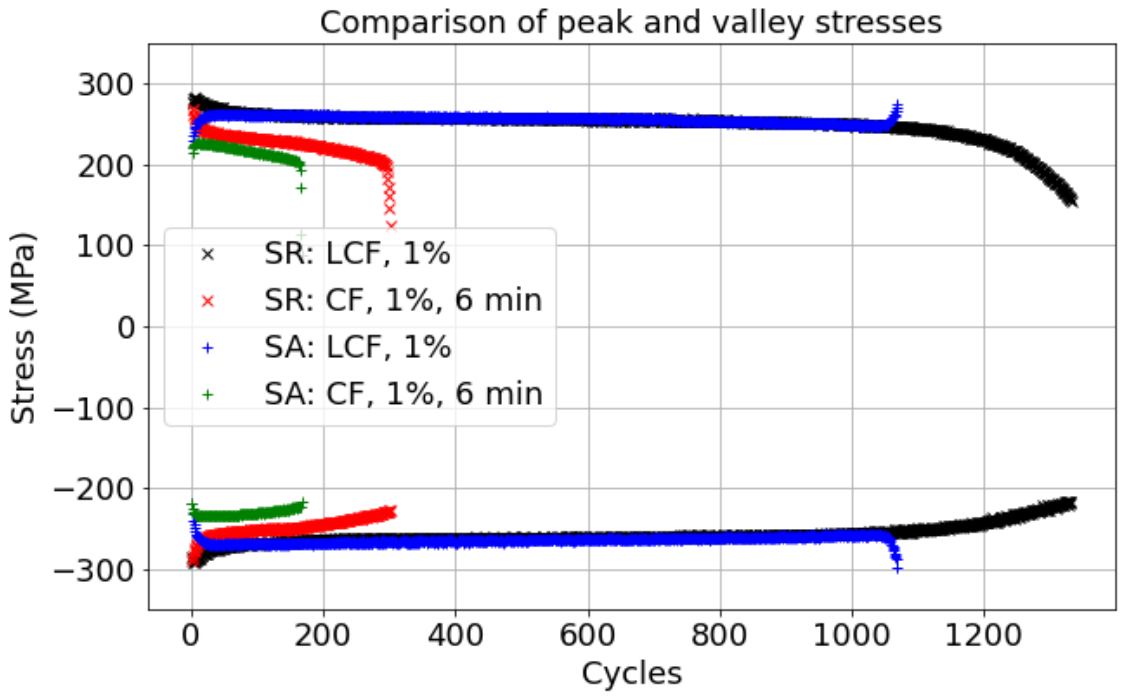

Figure 37. Comparison of the peak and valley stress plots from fatigue and creep-fatigue tests with 1% strain range at 650C.

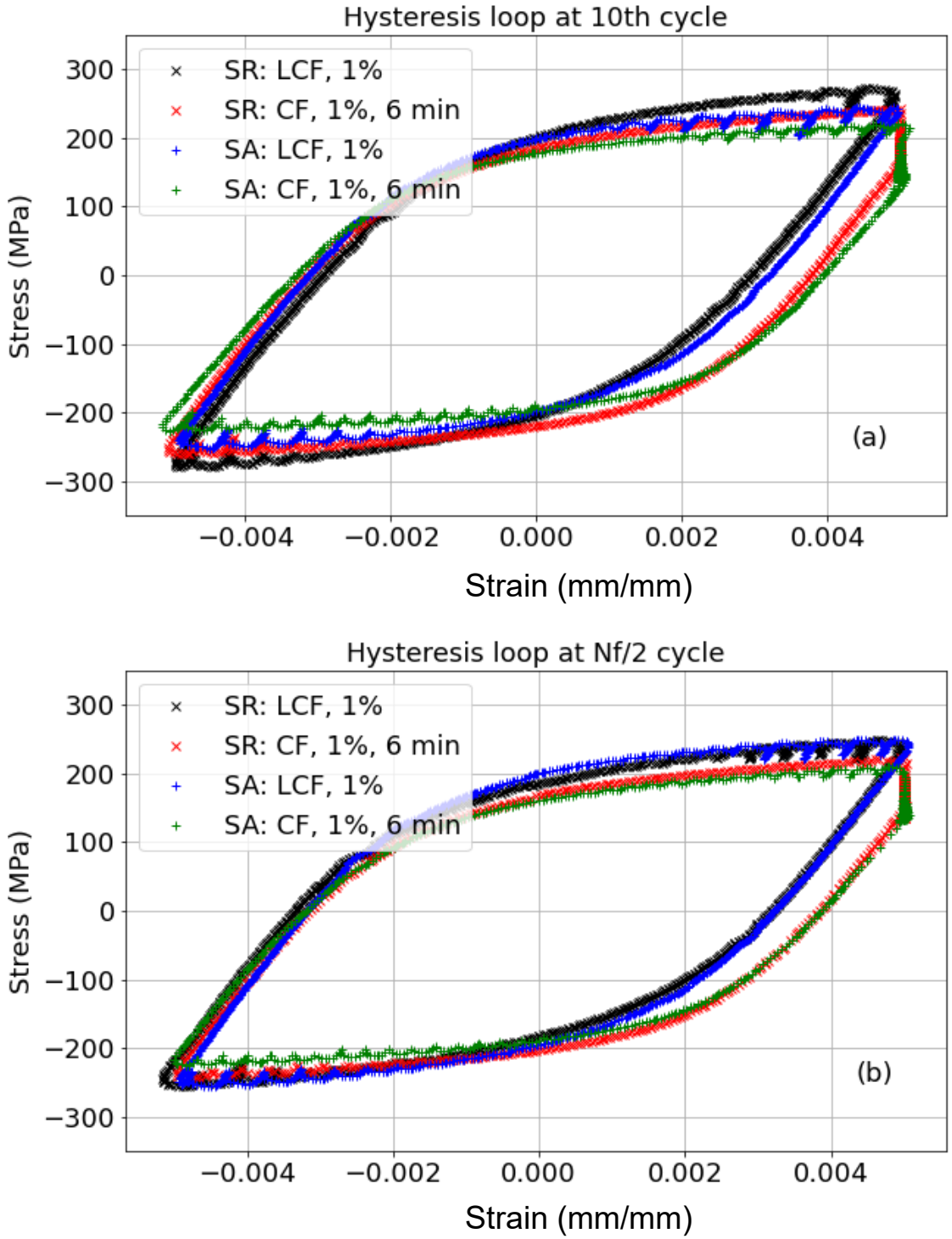

Figure 38. Comparison of hysteresis loops from (a) 10th cycle and (b) half-life from cyclic tests.

6.6 Conclusions from fatigue and creep fatigue tests of LPBF 316H

Major conclusions from fatigue and creep fatigue tests of LPBF 316H are:

- The differing cyclic responses observed among samples produced with different LPBF systems may stem from their laser temporal modes. Samples produced with continuous-wave lasers consistently exhibit better cyclic performance than those built with pulsed-wave lasers. The root cause of these performance differences remains unclear; additional testing and microstructural characterization are needed to isolate the laser-mode effect.
- To assess the effect of orientation on cyclic response, solution-annealed samples were tested in the transverse and build directions under near-identical conditions. Transverse specimens cyclically harden more but have shorter cyclic lives than build-direction specimens, consistent with creep results showing superior performance in the build direction.
- Acceptance tests per BPVC Section III, Division 5 on solution-annealed samples showed a dominant orientation effect with the build-direction samples outperformed the transverse samples with both CW and PW laser modes. While none of the tested samples pass the >200-cycle criterion, samples produced with CW laser in build direction are more promising to meet the requirement.
- Fatigue and creep-fatigue tests at 750°C exhibited cyclic stress relaxation consistent with prior 550–650°C results. The comparison between the creep-fatigue and fatigue hysteresis loops shows additional in-cycle strain accumulation during the hold in creep-fatigue tests. The extent of stress relaxation increases as the hold time increases from 6 to 30 minutes.

7 Conclusion and outlook

This study provides a comprehensive investigation of the high-temperature mechanical behavior and microstructural evolution of LPBF 316H SS. Key conclusions are:

- The SA condition of 1100°C, 1 hour was down-selected for the first ASME code case on LPBF 316H due to its better creep ductility compared to AB and SR conditions at high temperatures such as 800°C.
- The AB LPBF 316H exhibits precipitation kinetics that are 10–100 times faster than its wrought counterpart during thermal aging, due to the high densities of preferred nucleation sites and elemental segregation inherent to the LPBF process. A physics-informed model was developed to predict long-term precipitation evolution during thermal aging of AB LPBF 316H, which was used to model strength degradation. Despite this degradation, the model predicts that AB LPBF 316H will retain higher yield strength than wrought 316H SS over long-term service.
- Thermal aging study of SA LPBF 316H is ongoing, with initial results up to 2,500 hours showing high yield strength but low ultimate tensile strength, and poor ductility at 750°C.
- The creep rupture life of SA LPBF 316H SS is largely within the scatter band of wrought 316H SS, and it consistently demonstrates a lower minimum creep rate. However, a significant drop in creep ductility was observed at 800°C. Microstructural analysis of ruptured specimens revealed that this embrittlement is mechanistically linked to the accelerated formation of brittle sigma phase along the fine grain boundaries, which promotes intergranular crack propagation.
- The fatigue and creep-fatigue performance of LPBF 316H SS is highly sensitive to manufacturing parameters and specimen orientation. Materials produced with continuous-wave (CW) lasers consistently outperformed those made with pulsed-wave (PW) lasers. Furthermore, specimens tested along the build direction generally exhibited longer cyclic lives than those from the transverse direction. In long-hold-time (60 min) creep-fatigue "acceptance" tests conducted at 595°C with 0.5% strain amplitude, none of the SA samples lasted over 200 cycles, which fell below the acceptance criterion under the ASME BPVC Section III, Division 5 for WT 316H.

The results from FY25 have provided critical insights into the process-microstructure-property relationships of LPBF 316H SS, laying the groundwork for its qualification. The following activities are planned for FY26 to address the remaining knowledge gaps and challenges:

- Continued long-term testing: The ongoing mid-term creep tests (with target rupture times of thousands of hours) and the thermal aging studies on SA material (beyond 2,500 hours) will be completed. The data generated will be crucial for validating and refining the long-term performance prediction models.
- In-depth microstructural characterization: Detailed post-test characterization will be performed on the aged, creep-ruptured, and fatigue-tested specimens. This will focus on quantifying the precipitation kinetics in SA material and mechanistically understanding the observed effects of build orientations and batch variations on creep and cyclic performance.
- Materials optimization: Given that the current SA material has a significant creep ductility drop at high temperatures such as 800°C due to the formation of embrittling sigma phase along grain boundaries, future work will explore mitigation strategies such as sigma phase

prevention, grain boundary strengthening, and grain boundary engineering, without compromising other mechanical properties.

- Long-term performance prediction: The experimental data will be integrated into physics-based models (through a companion project under the AMMT program) to enhance their predictive accuracy for long-term strength, creep, and creep-fatigue behavior. This iterative process of model refinement and experimental validation is essential for establishing a robust rapid qualification framework.

Through these continued efforts, this project will advance the technical basis required for the accelerated codification and deployment of LPBF 316H SS in advanced nuclear reactors and other high-temperature applications.

Acknowledgement

The work of the ANL authors was sponsored by the U.S. Department of Energy, Office of Nuclear Energy, Advanced Materials and Manufacturing Technologies (AMMT) program, under Contract No. DE-AC02-06CH11357 with ANL, managed and operated by UChicago Argonne LLC. Work performed at the Center for Nanoscale Materials and the Advanced Photon source, both U.S. Department of Energy Office of Science User Facilities, was supported by the U.S. DOE, Office of Basic Energy Sciences, under Contract No. DE-AC02-06CH11357.

The work of the INL authors was sponsored by the U.S. Department of Energy, Office of Nuclear Energy, Advanced Materials and Manufacturing Technologies (AMMT) program under Contract No. DE-AC07-05ID14517 with INL, which is managed and operated by Battelle Energy Alliance.

The authors acknowledge support for this work from the AMMT program with programmatic guidance provided by Meimei Li at Argonne National Laboratory, Ryan Dehoff at Oak Ridge National Laboratory and Dirk Cairns-Gallimore at the Department of Energy.

The authors thank Edward Listwan, Jun-Sang Park, Robin Montoya, Caleb Massey, Peeyush Nandwana, Joel Simpson and Alex Pomo for technical supports and discussions.

References

[1] M. Li, D. Andersson, R. Dehoff, A. Jokisaari, I. van Rooyen, D. Cairns-Gallimore, Advanced Materials and Manufacturing Technologies (AMMT) 2022 Roadmap, Argonne National Lab. (ANL), Argonne, IL (United States), 2022. https://www.osti.gov/biblio/1958265 (accessed August 21, 2024).

[2] X. Zhang, L. Gao, S.A. Mantri, Technical basis for understanding the process-microstructure-property correlation in LPBF 316 SS, Argonne National Laboratory (ANL), Argonne, IL (United States), 2024. https://doi.org/10.2172/2467450.

[3] X. Zhang, Y. Chen, S.A. Mantri, L. Gao, E. Listwan, J. Listwan, M. McMurtrey, N. Mohale, C. Massey, FY24 Integrated Results for High-Temperature Mechanical Testing of LPBF 316H Stainless Steel, Argonne National Laboratory (ANL), Argonne, IL (United States). Center for Nanoscale Materials (CNM); Idaho National Laboratory (INL), Idaho Falls, ID (United States); Oak Ridge National Laboratory (ORNL), Oak Ridge, TN (United States), 2024. https://doi.org/10.2172/2447990.

[4] Standard Specification for Seamless Ferritic and Austenitic Alloy-Steel Boiler, Superheater, and Heat-Exchanger Tubes, (n.d.). https://www.astm.org/a0213_a0213m-22a.html (accessed August 20, 2024).

[5] P.C. Han, Q. Li, N.R. Tao, Strain partition induced abnormal low-cycle fatigue behavior in single-phase heterostructured 316L stainless steels, Scr. Mater. 227 (2023) 115274. https://doi.org/10.1016/j.scriptamat.2022.115274.

[6] BPVC Section III-Div 5 - High Temperature Reactors - ASME, (n.d.). https://www.asme.org/codes-standards/find-codes-standards/bpvc-iii-5-bpvc-section-iii-rules-construction-nuclear-facility-components-division-5-high-temperature-reactors (accessed November 6, 2024).

[7] M. Li, W.-Y. Chen, Microstructure-based prediction of thermal aging strength reduction factors for grade 91 ferritic-martensitic steel, Mater. Sci. Eng. A 798 (2020) 140116. https://doi.org/10.1016/j.msea.2020.140116.

[8] L.P. Stoter, Thermal ageing effects in AISI type 316 stainless steel, J. Mater. Sci. 16 (1981) 1039–1051. https://doi.org/10.1007/BF00542750.
[9] V.K. Sikka, Effects of thermal aging on the mechanical properties of type 316 stainless steel - elevated-temperature properties, Oak Ridge National Lab. (ORNL), Oak Ridge, TN (United States), 1982. https://doi.org/10.2172/708800.
[10] J.A. Horak, V.K. Sikka, D.T. Raske, Review of effects of long-term aging on the mechanical properties and microstructures of Types 304 and 316 stainless steel, Oak Ridge National Lab., TN (USA); Argonne National Lab., IL (USA), 1985. https://www.osti.gov/biblio/5393022 (accessed February 19, 2025).
[11] J.H. Hollomon, L.D. Jaffe, Time-temperatures relations in tempering steel, Trans. Am. Inst. Min. Metall. Eng. 162 (1945) 223–249.
[12] P. Deng, M. Karadge, R.B. Rebak, V.K. Gupta, B.C. Prorok, X. Lou, The origin and formation of oxygen inclusions in austenitic stainless steels manufactured by laser powder bed fusion, Addit. Manuf. 35 (2020) 101334. https://doi.org/10.1016/j.addma.2020.101334.
[13] B. Weiss, R. Stickler, Phase instabilities during high temperature exposure of 316 austenitic stainless steel, Metall. Trans. 3 (1972) 851–866. https://doi.org/10.1007/BF02647659.
[14] E.H. Lee, P.J. Maziasz, A.F. Rowcliffe, Structure and composition of phases occurring in austenitic stainless steels in thermal and irradiation environments, Oak Ridge National Lab., TN (USA), 1980. https://www.osti.gov/biblio/5889791 (accessed August 20, 2024).
[15] J.K.L. Lai, A review of precipitation behaviour in AISI type 316 stainless steel, Mater. Sci. Eng. 61 (1983) 101–109. https://doi.org/10.1016/0025-5416(83)90191-X.
[16] B. Weiss, R. Stickler, Phase instabilities during high temperature exposure of 316 austenitic stainless steel, Metall. Trans. 3 (1972) 851–866. https://doi.org/10.1007/BF02647659.
[17] THE CORPUSCLE PROBLEM. A MATHEMATICAL STUDY OF A BIOMETRIC PROBLEM | Biometrika | Oxford Academic, (n.d.). https://academic.oup.com/biomet/article-abstract/17/1-2/84/215917?redirectedFrom=fulltext (accessed July 30, 2025).
[18] C.V. Funch, F.B. Grumsen, A.B. da S. Fanta, T.L. Christiansen, M.A.J. Somers, Thermal stability of hierarchical microstructural features in additively manufactured stainless steel, Heliyon 9 (2023). https://doi.org/10.1016/j.heliyon.2023.e16555.
[19] MICROGRAPHS AND MICROSTRUCTURAL CHARACTERISTICS OF CREPT SPECIMENS OF 18Cr-12Ni-Mo STAINLESS STEEL FOR BOILER AND HEAT EXCHANGER SEAMLESS TUBES (SUS 316H TB), NIMS Creep Data Sheet Metallogr. Atlas Long-Term Crept Mater. (2003) 86.
[20] S. Dixit, S. Liu, H.A. Murdoch, P.M. Smith, Investigating build orientation-induced mechanical anisotropy in additive manufacturing 316L stainless steel, Mater. Sci. Eng. A 880 (2023) 145308. https://doi.org/10.1016/j.msea.2023.145308.
[21] A. Charmi, R. Falkenberg, L. Ávila, G. Mohr, K. Sommer, A. Ulbricht, M. Sprengel, R. Saliwan Neumann, B. Skrotzki, A. Evans, Mechanical anisotropy of additively manufactured stainless steel 316L: An experimental and numerical study, Mater. Sci. Eng. A 799 (2021) 140154. https://doi.org/10.1016/j.msea.2020.140154.
[22] J. Hu, G. Green, S. Hogg, R. Higginson, A. Cocks, Effect of microstructure evolution on the creep properties of a polycrystalline 316H austenitic stainless steel, Mater. Sci. Eng. A 772 (2020) 138787. https://doi.org/10.1016/j.msea.2019.138787.

[23] T. Hu, H.H.J. Choi, M.C. Messner, A mechanistic model for creep and thermal aging in Alloy 709, Argonne National Laboratory (ANL), Argonne, IL (United States), 2023. https://doi.org/10.2172/1999400.
[24] M. Perez, M. Dumont, D. Acevedo-Reyes, Implementation of classical nucleation and growth theories for precipitation, Acta Mater. 56 (2008) 2119–2132. https://doi.org/10.1016/j.actamat.2007.12.050.
[25] P.G. Shewmon, Transformations in Metals, McGraw-Hill, 1969.
[26] R. Pokharel, A. Patra, D.W. Brown, B. Clausen, S.C. Vogel, G.T. Gray, An analysis of phase stresses in additively manufactured 304L stainless steel using neutron diffraction measurements and crystal plasticity finite element simulations, Int. J. Plast. 121 (2019) 201–217. https://doi.org/10.1016/j.ijplas.2019.06.005.
[27] A.A. Kohnert, L. Capolungo, The kinetics of static recovery by dislocation climb, Npj Comput. Mater. 8 (2022) 104. https://doi.org/10.1038/s41524-022-00790-y.
[28] G.E. Lucas, The evolution of mechanical property change in irradiated austenitic stainless steels, J. Nucl. Mater. 206 (1993) 287–305. https://doi.org/10.1016/0022-3115(93)90129-M.
[29] X. Zhang, C. Xu, Y. Chen, W.-Y. Chen, J.-S. Park, P. Kenesei, J. Almer, J. Burns, Y. Wu, M. Li, High-energy synchrotron x-ray study of deformation-induced martensitic transformation in a neutron-irradiated Type 316 stainless steel, Acta Mater. 200 (2020) 315–327. https://doi.org/10.1016/j.actamat.2020.08.057.
[30] H. Sieurin, J. Zander, R. Sandström, Modelling solid solution hardening in stainless steels, Mater. Sci. Eng. A 415 (2006) 66–71. https://doi.org/10.1016/j.msea.2005.09.031.
[31] I.K. J, The Strength of Austenitic Stainless Steels, J Iron Steel Inst 207 (1969) 1017–1028.
[32] S. Queyreau, G. Monnet, B. Devincre, Orowan strengthening and forest hardening superposition examined by dislocation dynamics simulations, Acta Mater. 58 (2010) 5586–5595. https://doi.org/10.1016/j.actamat.2010.06.028.
[33] M. Jiang, X. Zhang, H. Mei, S. Xu, L. Liu, The coupled effects of grain boundary strengthening and Orowan strengthening examined by dislocation dynamics simulations, Comput. Mater. Sci. 231 (2024) 112602. https://doi.org/10.1016/j.commatsci.2023.112602.
[34] U.F. Kocks, The theory of an obstacle-controlled yield strength—Report after an international workshop, Mater. Sci. Eng. 27 (1977) 291–298. https://doi.org/10.1016/0025-5416(77)90212-9.
[35] X. Zhang, L. Gao, S.A. Mantri, Technical basis for understanding the process-microstructure-property correlation in LPBF 316 SS, Argonne National Laboratory (ANL), Argonne, IL (United States), 2024. https://doi.org/10.2172/2467450.
[36] L. Gao, S.A. Mantri, X. Zhang, Quantification of solution annealing effects on microstructure and property in a laser powder bed fusion 316H stainless steel, Mater. Des. 251 (2025) 113692. https://doi.org/10.1016/j.matdes.2025.113692.
[37] M.C. Messner, X. Zhang, Y. Chen, C. Massey, M. McMurtrey, R.A. Montoya, M.J. Brand, O.R. Mireles, K. Le, Updated ASME design correlations and qualification plan for powder bed fusion 316H stainless steel, Argonne National Lab. (ANL), Argonne, IL (United States), 2024.
[38] M. Petkov, P.-A. Juan, Revised creep fracture maps of Type 316 stainless steel and their mechanistic perspective, Eng. Fail. Anal. 159 (2024) 108094. https://doi.org/10.1016/j.engfailanal.2024.108094.

Nuclear Science and Engineering
Argonne National Laboratory
9700 South Cass Avenue, Bldg. 212
Argonne, IL 60439

www.anl.gov

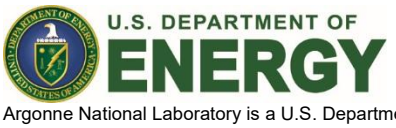

Argonne National Laboratory is a U.S. Department of Energy laboratory managed by UChicago Argonne, LLC